

# Interference and Transmission of Locally Forced Internal Waves in Non-Uniform Stratifications

by

Rohit B. Supekar

B.Tech., Indian Institute of Technology Madras (2015)

Submitted to the Department of Mechanical Engineering  
in partial fulfillment of the requirements for the degree of

Master of Science in Mechanical Engineering

at the

MASSACHUSETTS INSTITUTE OF TECHNOLOGY

June 2017

© Massachusetts Institute of Technology 2017. All rights reserved.

**Signature redacted**

Author .....

.....  
Department of Mechanical Engineering

May 12, 2017

**Signature redacted**

Certified by...

.....

Thomas Peacock

Professor

Thesis Supervisor

**Signature redacted**

Accepted by .....

.....  
Rohan Abeyaratne

Chairman, Department Committee on Graduate Theses





# Interference and Transmission of Locally Forced Internal Waves in Non-Uniform Stratifications

by

Rohit B. Supekar

Submitted to the Department of Mechanical Engineering  
on May 12, 2017, in partial fulfillment of the  
requirements for the degree of  
Master of Science in Mechanical Engineering

## Abstract

Several studies have investigated the effect of constructive or destructive interference on the transmission of internal waves that propagate through non-uniform stratifications. Such studies have been performed for internal waves that are spatiotemporally harmonic. To understand the effect of spatiotemporal localization, this thesis presents a theoretical and experimental study of the transmission of two-dimensional internal waves that are generated by a boundary forcing that is localized in both space and time. This is done by considering an idealized problem and applying a weakly viscous semi-analytic linear model to it. After validation with a numerical model, the semi-analytic model allows us to perform parametric studies.

Using theoretical studies, we show that localization leads to the disappearance of transmission peaks and troughs that would otherwise be present for a harmonic forcing. The laboratory experiments that we perform provide a clear indication of this physical effect. Based on the group velocity and angle of propagation of the internal waves, a practical criteria that assesses when the transmission peaks or troughs are evident, is obtained. It is found that there is a significant difference in the predicted energy transfer due to a harmonic and non-harmonic forcing which has direct implications to various physical forcings such as a storm over the ocean.

Thesis Supervisor: Thomas Peacock

Title: Professor



## Acknowledgments

First and foremost, I thank Professor Tom Peacock for providing his invaluable guidance and physical insight throughout my research at MIT. I deeply appreciate his willingness to help me with any minute technicalities and yet provide me with the required independence whenever needed. I also want to extend my gratitude to Professor Mahesh Panchagnula, my advisor from undergraduate studies at IIT Madras, who got me interested in the field of Fluid Mechanics. To this date, I often fall back to the numerous ways in which he taught me to think about scientific questions.

I convey special thanks to Sasan Ghaemsaidi for getting me started with internal waves research in my first semester and Paco Maurer for providing some of the initial codes for this work. I also appreciate the assistance of Lorraine Rabb and Leslie Regan in administrative matters.

Over the past two years, ENDLab-mates and Nexus-mates have created an enjoyable work environment. It has always been fun to take a break from research and have very insightful discussions on fairly arbitrary topics. Many cheers to all the fellow runners and coaches at my running club, the Community Running Association! The Monday and Wednesday night workouts have, without fail, made the earlier part of any week much nicer.

Neha, I do not have enough words to describe how much your unparalleled support has meant to me over the last five years. You have played an instrumental role in getting me where I am today and I will always be grateful to you for that.

A very special mention goes to all my close friends at MIT and all around the world for their delightful company and help in times of need. And finally, last but by no means the least, I want to thank my loving parents and sister for constantly believing in me. The presence of close friends and family is what makes all of this meaningful and important.

This work was supported by the NSF OCE 1357434 grant.



# Contents

|          |  |           |
|----------|--|-----------|
| <b>1</b> | <b>Introduction</b>  | <b>17</b> |
| 1.1      | Internal Waves . . . . .                                       | 17        |
| 1.1.1    | Stratified Fluids . . . . .                                    | 17        |
| 1.1.2    | Internal Waves in the Océan and the Atmosphere . . . . .       | 19        |
| 1.2      | Internal Wave Interference . . . . .                           | 20        |
| 1.2.1    | Previous Work . . . . .  | 20        |
| 1.2.2    | Current Work . . . . .   | 21        |
| 1.3      | Thesis Outline . . . . .                                       | 22        |
| <b>2</b> | <b>Mathematical Model</b>                                      | <b>23</b> |
| 2.1      | Governing Equations for Internal Waves . . . . .               | 23        |
| 2.1.1    | Dispersion Relation . . . . .                                  | 25        |
| 2.2      | Problem Formulation . . . . .                                  | 25        |
| 2.3      | Solution Procedure by Fourier Decomposition . . . . .          | 28        |
| 2.4      | Numerical Model . . . . .                                      | 31        |
| <b>3</b> | <b>Theoretical Results</b>                                     | <b>33</b> |
| 3.1      | Validation Case Study . . . . .                                | 33        |
| 3.1.1    | Comparison with Numerical Model Results . . . . .              | 35        |
| 3.2      | Effects of Spatiotemporal Localization . . . . .               | 37        |
| 3.2.1    | Criteria for Possible Interference Effects . . . . .           | 37        |
| 3.2.2    | Comparison of Harmonic and Non-Harmonic Transmission . . . . . | 39        |
| 3.3      | Conclusions . . . . .  | 41        |

|  |           |
|--|-----------|
| <b>4 Experiments</b>                       | <b>43</b> |
| 4.1 Apparatus . . . . .                    | 43        |
| 4.2 Wave Generator Configuration . . . . . | 46        |
| 4.3 Results . . . . .                      | 48        |
| 4.3.1 Transmission Studies . . . . .       | 49        |
| 4.3.2 Discussion . . . . .                 | 51        |
| <b>5 Conclusions</b>                       | <b>57</b> |
| 5.1 Future Work . . . . .                  | 59        |

# List of Figures

|     |   |    |
|-----|---|----|
| 1-1 | Schematic of buoyancy-driven oscillations of a fluid parcel about $z = z_0$ in a linearly stratified medium. $F_B$ indicates the upward buoyancy force (in red) and $F_g$ indicates the downward gravitational force (in black) on the fluid parcel. The vertical position of the parcel is indicated as time progresses (rightwards). The arrows indicate the relative magnitudes of the forces. . . . .   | 18 |
| 1-2 | Stratification profile from the equatorial Pacific ocean ( $0.5^\circ N, 149.5^\circ E$ ) averaged over the month of April in 2015. In order from left to right, the panels plot the salinity $S$ (psu), potential temperature $T$ ( $^\circ C$ ), potential density $\bar{\rho}$ ( $kg\ m^{-3}$ ) and the buoyancy frequency $N$ ( $s^{-1}$ ). The salinity and temperature were obtained from the climatology data by Roemmich & Gilson (2009). The potential density and buoyancy frequency were then calculated using the Gibbs Seawater Toolbox (McDougall & Barker (2011)). . . . . | 20 |
| 2-1 | Sketch of the physical system. The colored solid lines indicate the vertical velocity forcing function at times $t_-$ (red), $t_0$ (green) and $t_+$ (blue) such that $t_- < t_0 < t_+$ . The dotted lines indicate the corresponding Gaussian envelopes. Solid lines with arrows define approximate boundaries of the internal wave packets, while the arrows indicate the direction of the group velocity. . . . .  | 26 |

|     |   |    |
|-----|---|----|
| 2-2 | An example forcing function and its corresponding Fourier spectra. The left panel indicates the localized nature of the forcing in the spatial dimension $x$ and the temporal dimension $t$ . Lines of constant phase have the same slope in the entire domain. The right panel indicates the Fourier spectra of this forcing. It is a Gaussian blob with a peak at $(k_0, \omega_0)$ . Its widths are inversely proportional to $\sigma_t$ and $\sigma_x$ . . . . .                                | 28 |
| 2-3 | The domain used for the nonlinear simulations. No-slip or zero-valued Dirichlet boundary conditions are applied at the boundaries A, B and C. At the top boundary D, the vertical velocity is set to the forcing function as indicated and the horizontal velocity is set to zero. Arrows indicate the forcing velocity vectors. . . . .  | 32 |
| 3-1 | Forcing and the excited vertical velocity field for validation case study at $tN_1 = 135$ . a) Spatiotemporal nature of the velocity forcing at $z = 0$ , wherein the horizontal line indicates the current time. b) Vertical velocity field in the domain at the current time. The arrows indicate the group velocities of the respective wave packets. c) Stratification or the buoyancy frequency profile. Dotted lines in panel b indicate the transition region of the stratification. . . . . | 34 |
| 3-2 | Comparison of the semi-analytic and numerical vertical velocity field normalized by the forcing amplitude $(w/A)$ at $tN_1 = 135$ . The dotted lines in both the panels indicate the transition region of the background stratification . . . . .   | 35 |
| 3-3 | Comparison of the normalized Fourier spectra of the vertical velocity obtained from the semi-analytic model and numerics (for the same parameters as in figure (3-1) with $tN_1 = 135$ ). Panel (a): above the transition layer, panel (b): inside the transition layer and panels (c, d): below the transition layer. . . . .  | 36 |

|     |  |    |
|-----|--|----|
| 3-4 | Sketch of the physical system overlaid with the length scale $L^*$ and the distance $L_0$ . Arrows associated with the waves indicate the direction of the group velocity. . . . .   | 38 |
| 3-5 | Comparison of the transmission parameter (for $\Delta/L = 0.5$ , $N_2/N_1 = 0.6$ ) in the harmonic and non-harmonic case. The left panel shows the transmission parameter for harmonic forcing. The black circles in both the panels indicate the forcing parameters considered for the motivating example. The right panel shows the transmission parameter for a localized forcing with $\sigma_t N_1 = 22.5$ , $\sigma_x/L = 2$ . . . . . | 39 |
| 3-6 | Effect of temporal delocalization on the transmission parameter and the total energy transferred (for $\Delta/L = 0.5$ , $N_2/N_1 = 0.6$ , $\sigma_x/L = 2$ , $k_0 L = 4$ ) . The color bar in the left panel is set to be the same as in figure (3-5). The contours in both the panels correspond to the function $\min\{n_x, n_t\}$ . . . . .  | 40 |
| 4-1 | Schematic of the front view of the experimental setup. The observation region is indicated by dotted lines and it is illuminated from underneath the tank by the LASER sheet (depicted in green). . . . .  | 44 |
| 4-2 | Actual experimental setup indicating all the important components . . . . .  | 44 |
| 4-3 | Experimental stratification profile. The left panel indicates the density variation that is measured using the conductivity probe. The right panel shows the buoyancy frequency profile obtained by numerical differentiation of the raw density profile. The fitted analytic function to this profile is also indicated. . . . .  | 46 |

|     |   |    |
|-----|---|----|
| 4-4 | An example of the temporal part of the wave generator forcing given by equation (4.3). Panel a shows the angular velocity ( $d\gamma/dt$ ) of the motor for the following set of experimental parameters: $\omega_0 = 0.68 \text{ s}^{-1}$ , $\sigma_t = 50 \text{ s}$ , $t_0 = 40 \text{ s}$ , $\delta = 20 \text{ s}$ , $e = 5 \text{ mm}$ . Panel b indicates the vertical position and velocity of a single generator plate. Panel c shows the amplitude of the Fourier Transform of the plate vertical velocity $w_j$ , wherein the dotted red lines indicate $\pm\omega_0$ . . . . .  | 47 |
| 4-5 | Theoretical and experimental transmission for different values of the temporal parameters $\sigma_t$ and $\omega_0$ . In panel a, the red, blue and green solid lines indicate the transmission computed by using the semi-analytic model for a spatiotemporally localized forcing. The solid black line indicates the transmission for a harmonic forcing ( $\sigma_x, \sigma_t \rightarrow \infty$ ). In panel b, the star markers are the experimental transmission values with the colors corresponding to the respective $\sigma_t$ values. The vertical dotted lines in both the panels indicate the buoyancy frequencies in the lower and upper layer ( $N_2$ and $N_1$ ). . . . . | 50 |
| 4-6 | Plots of the experimental vertical velocity field normalized by the forcing amplitude ( $w/(A\omega_0)$ ). All the panels indicate velocity fields forced at $\omega_0 = 0.68 \text{ s}^{-1}$ , a frequency at which resonance occurs. Rows a, b and c indicate velocity fields for $\sigma_t = 20, 50$ and $200 \text{ s}$ respectively. The left and right panels of each row correspond to the velocity field at the time $t_0$ (about which the angular velocity is symmetric) and at $40 \text{ s}$ after $t_0$ . . . . .  | 52 |
| 4-7 | Plots of the experimental vertical velocity field normalized by the forcing amplitude ( $w/(A\omega_0)$ ). All the panels indicate velocity fields forced at $\omega_0 = 0.86 \text{ s}^{-1}$ , a frequency at which diminution occurs. Rows a, b and c indicate velocity fields for $\sigma_t = 20, 50$ and $200 \text{ s}$ respectively. The left and right panels of each row correspond to the velocity field at the time $t_0$ (about which the angular velocity is symmetric) and at $40 \text{ s}$ after $t_0$ . The color scale is the same as in figure (4-6). . . . .   | 53 |

4-8 Plots of the critical ratios  $n_x$  and  $n_t$ . The left panel presents the plots of  $n_x$  (solid black line) and  $n_t$  (solid colored lines).  $n_t$  is plotted for different values of  $\sigma_t$ . The right panel indicates the minimum of  $n_x$  and  $n_t$ . A log scale is used for the y-axis. In both the panels, the black dotted line indicates the value of 1.5 for reference. . . . . 55



# List of Tables

|     |   |    |
|-----|---|----|
| 4.1 | Values chosen for temporal forcing parameters: $\sigma_t$ , $\delta$ and $t_0$ for the experiments. . . . . | 49 |
|-----|---|----|



# Chapter 1

## Introduction

This thesis presents a study of the effect of spatiotemporal localization of a boundary forcing on the transmission of internal waves through non-uniform stratifications. In this chapter, we describe the importance of internal waves in section (1.1). Previous work in the area of internal wave interference is presented in section (1.2.1) and the distinction of the current work is presented in section (1.2.2). Finally, the outline of the thesis is discussed in section (1.3).

### 1.1 Internal Waves

#### 1.1.1 Stratified Fluids

Fluids are termed to be ‘stratified’ if they have density variations with depth. If the density increases monotonically with depth, they are gravitationally stable and are often referred to as ‘statically stable’. Since it costs energy to move fluid parcels up or down due to gravitational and buoyancy forces respectively, stratified fluids tend to move in horizontal layers. If provided with an adequate amount of energy through a forcing, however, they can allow for waves to propagate through them.

To understand how a stratified fluid supports waves, consider a fluid parcel in a stratified fluid as shown in figure (1-1). Due to some forcing, the fluid parcel is initially perturbed vertically upwards by a distance  $\delta$  from its neutrally buoyant location

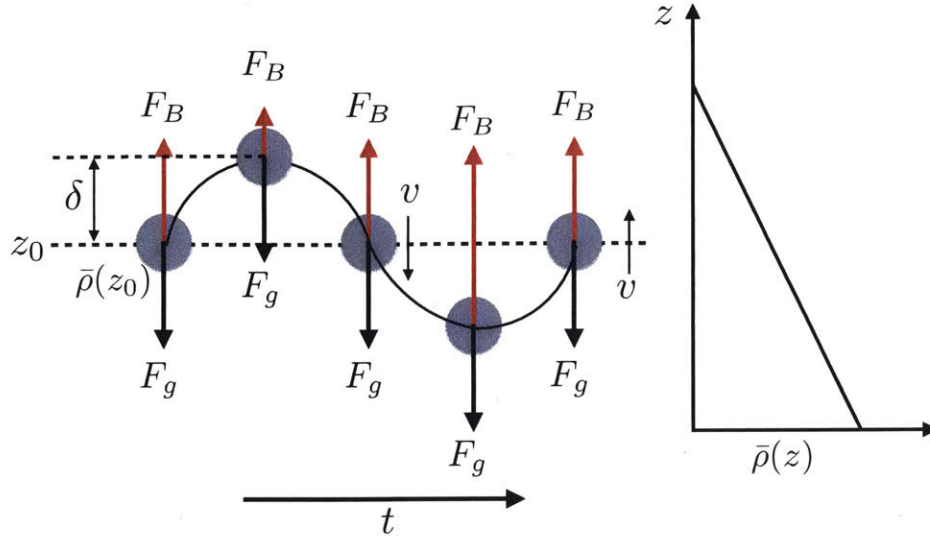


Figure 1-1: Schematic of buoyancy-driven oscillations of a fluid parcel about  $z = z_0$  in a linearly stratified medium.  $F_B$  indicates the upward buoyancy force (in red) and  $F_g$  indicates the downward gravitational force (in black) on the fluid parcel. The vertical position of the parcel is indicated as time progresses (rightwards). The arrows indicate the relative magnitudes of the forces.

$z = z_0$ . Because of the stratification, this parcel then feels a larger gravitational force than the buoyancy force. As a result, the parcel is pulled backwards to the original position. When it overshoots its original position, the buoyancy force overcomes the gravitational force and the parcel experiences a net upward force. This is similar to the action of a spring on a mass. Thus, the equation of motion for a single fluid parcel can be written as follows:

$$\frac{d^2 z_p}{dt^2} - \frac{g}{\rho_0} \frac{d\bar{\rho}}{dz} z_p = 0. \quad (1.1)$$

In equation (1.1),  $z_p$  indicates the vertical position of the fluid parcel,  $\bar{\rho}(z)$  is the density profile in the fluid,  $g$  is the gravitational acceleration and  $\rho_0$  is a characteristic density of the fluid. The 2nd term on the left hand side indicates the difference between the buoyancy and gravitational forces for a given displacement  $z_p$ . Clearly, this equation admits oscillatory solutions with a natural frequency given by:

$$N = \sqrt{-\frac{g}{\rho_0} \frac{d\bar{\rho}}{dz}}. \quad (1.2)$$

This natural frequency is often referred to as the Brunt-Väisälä frequency or the buoyancy frequency. Such buoyancy-driven oscillations give rise to waves in the interior of a stratified fluid. These are thus termed as ‘internal’ waves.

### 1.1.2 Internal Waves in the Ocean and the Atmosphere

The ocean and atmosphere are naturally stratified mediums. Density changes in the ocean are caused by variations in salinity and temperature. In the atmosphere, density variations are majorly due to temperature and pressure changes. In both the ocean and the atmosphere, it is more common than rare to encounter density changes that have a non-linear dependence on depth. This implies that the buoyancy frequency given by equation (1.2) is usually non-uniform. Specifically, for the ocean water column, the upper 100 m doesn’t have much density variation due to turbulence generated by wind or cyclonic activity (Toffoli *et al.* (2012)). This upper layer is usually referred to as the ‘mixed layer’ which has a buoyancy frequency close to zero. Below the mixed layer, there are large variations in the density which result in higher values of the buoyancy frequency (the pycnocline), below which lies the deep ocean with a relatively weak stratification (Gill (1982), Cushman-Roisin & Beckers (2011)). A typical stratification profile from the equatorial Pacific ocean is plotted in figure (1-2).

Internal waves manifest in the ocean and atmosphere through a variety of generation mechanisms. In the atmosphere, winds blowing over topography can generate low-frequency internal waves widely known as lee waves (Bell (1975), Baines & Hoinka (1985)). In the ocean, surface excitation of the mixed layer by storms excites strong near-inertial wave activity (Gill (1984), Alford *et al.* (2016)). In propagating downwards, these internal waves must traverse the pycnocline, or even more complex structures such as multiple pycnoclines and double-diffusive staircase structures that are known to exist in the central Canada Basin of the Arctic ocean (Timmermans *et al.* (2008)). Apart from surface storms and wind forcings, another important generation mechanism for internal waves in the ocean is through tidal oscillations over topography (Wunsch (1975), Echeverri & Peacock (2010)). It has been estimated

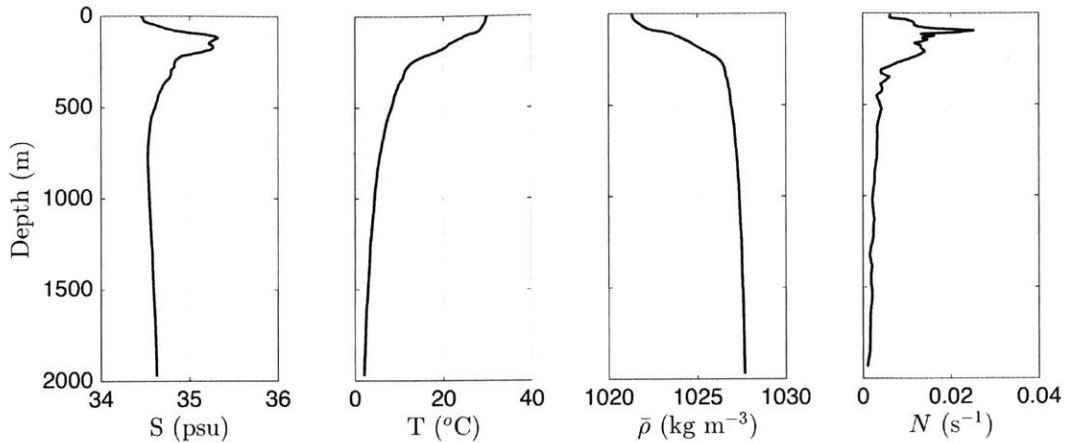


Figure 1-2: Stratification profile from the equatorial Pacific ocean ( $0.5^{\circ}N, 149.5^{\circ}E$ ) averaged over the month of April in 2015. In order from left to right, the panels plot the salinity  $S$  (psu), potential temperature  $T$  ( $^{\circ}C$ ), potential density  $\bar{\rho}$  ( $kg\ m^{-3}$ ) and the buoyancy frequency  $N$  ( $s^{-1}$ ). The salinity and temperature were obtained from the climatology data by Roemmich & Gilson (2009). The potential density and buoyancy frequency were then calculated using the Gibbs Seawater Toolbox (McDougall & Barker (2011)).

by Wunsch & Ferrari (2004) that both the surface wind forcings and tides have an almost equal part in the generation of internal waves in the ocean.

## 1.2 Internal Wave Interference

### 1.2.1 Previous Work

The propagation characteristics of internal waves such as their group velocity and propagation direction are strongly dependent on the buoyancy frequency of the stratified medium. In non-uniform stratifications, internal waves can be partially reflected and transmitted at interfaces of layers with unequal buoyancy frequencies or in layers with strong continuous variations in the buoyancy frequency (Sutherland (2010)). The reflected and incident waves can subsequently interfere with each other. As the ocean and the atmosphere are non-uniformly stratified, the study of constructive and destructive interference underlies our understanding of the passage of internal waves in these mediums. With this motivation, transmission coefficients for spatially and

temporally harmonic internal waves propagating through stratifications with discontinuous buoyancy frequency profiles were obtained by the insightful study of Sutherland & Yewchuk (2004). Thereafter, Nault & Sutherland (2007) further developed the methodology to address continuously varying stratifications.

Advancement in terms of localized internal waves was done by Mathur & Peacock (2009) who considered internal wave fields that were spatially localized, for the purpose of studying the propagation of internal wave beams through non-uniform stratifications. And most recently, utilizing such methods, a study by Ghaemsaidi *et al.* (2016a) has shown that multi-layered stratifications have a rich transmission behavior for internal waves that are spatially and temporally harmonic; multiple transmission peaks can exist due to constructive and destructive interference effects between propagating and evanescent waves (Ghaemsaidi (2015)). As a point of scientific interest, under certain circumstances these interference effects have a direct mathematical analogy to optical interferometry (Mathur & Peacock (2010)).

### 1.2.2 Current Work

In all of the studies mentioned in the previous section, although spatial localization was considered, the internal wave field was temporally harmonic. Since interference effects are due to the interactions of incident and reflected waves, however, both localization in space and in time are clearly important in determining whether interference effects will play a role for a given excitation.

Ghaemsaidi (2015) was the first to consider the problem of boundary-forced internal waves in non-uniform stratifications. In such a scenario, because internal waves are continuously forced, it was shown that a significant amplification leading up to resonance was possible. Separate studies were performed for continuous and discontinuous buoyancy frequency profiles. For the discontinuous stratification scenario, physical insight into this amplification process was obtained by considering the propagation of internal waves along ray paths (Sutherland (2010)). An analytical expression for the transmission as a function of the number of interactions between the reflected waves and the forcing was derived. As the number of interactions increases, this expression

converges to the one obtained for a harmonic forcing. This study thus suggests that the transmission of internal waves must get affected for forcings that are spatiotemporally localized. Such localized forcings are especially important as they are relevant in physical scenarios such as an ocean storm.

The above considerations motivate us to extend the problem discussed by Ghaemsaïdi (2015) to analyze how internal wave interference is affected by spatiotemporal localization. This is done by using the same physical setup but by replacing the harmonic forcing function with a quasi-monochromatic wave packet in a spatial and temporal sense. This introduces a band of frequencies and wavenumbers around the dominant values. Such a forcing is applied to a two-layered stratified fluid that has a finite transition layer where the buoyancy frequency changes continuously. The ray approach discussed by Ghaemsaïdi (2015) is used to identify the correct length and time scales for the forcing such that the effects of interference are evident leading up to developing a practical criteria.

### 1.3 Thesis Outline

The specific problem of boundary-forced internal waves in non-uniform stratifications is studied by utilizing semi-analytic, numerical and experimental techniques. We first present the idealized physical problem in chapter 2. The underlying semi-analytic model is also presented in this chapter, along with details of an accompanying numerical model. In chapter 3, we present a case study of a motivating example which was used to validate the internal wave fields obtained from our semi-analytic model against the numerical model. With this validation, we were able to perform parametric studies of the effects of spatiotemporal localization on internal wave interference by using the numerically cheap semi-analytic model. The results of this parametric study are also presented in chapter 3. Furthermore, a practical criteria to determine when the effects of interference are evident is developed. We demonstrate our predictions via a set of laboratory experiments, the results of which are presented in chapter 4. Finally, we present our conclusions in chapter 5.

# Chapter 2

## Mathematical Model

In this chapter, we discuss the mathematical framework that is used to make theoretical predictions about the transmission of boundary-forced internal waves. We start by deriving the governing equations of Boussinesq linear internal waves in section (2.1). The specific idealized problem under consideration is then described in section (2.2). Section (2.3) then presents the solution procedure we follow to solve the governing equations for our physical problem. To validate this semi-analytic linear model, the numerical model that we use is described in section (2.4).

### 2.1 Governing Equations for Internal Waves

Consider a stratified fluid whose background density changes as  $\bar{\rho}(z)$ , where the  $z$  axis is anti-parallel to gravity. For a gravitationally stable fluid, we require that  $d\bar{\rho}/dz < 0$ . For a Boussinesq fluid, we now write down the equations of motion in 2 dimensions. Under the Boussinesq approximation, the velocity field ( $\vec{u} = (u, w)$ ) must be divergence free (Kundu *et al.* (2012)).

$$\nabla \cdot \vec{u} = 0. \tag{2.1}$$

Assuming the Schmidt number ( $Sc = \nu/D$ , where  $\nu$  is the kinematic viscosity and  $D$  is the mass diffusivity) to be infinity, we also have the following requirement for the

density field  $\rho$ :

$$\frac{D\rho}{Dt} = 0; \quad (2.2)$$

here,  $D/Dt = \partial/\partial t + \vec{u} \cdot \nabla$ .

The fluid motion is governed by the Navier-Stokes equations as follows:

$$\frac{Du}{Dt} = -\frac{1}{\rho_0} \frac{\partial p}{\partial x} + \nu \nabla^2 u, \quad (2.3a)$$

$$\frac{Dw}{Dt} = -\frac{1}{\rho_0} \frac{\partial p}{\partial z} + \nu \nabla^2 w - \frac{\rho}{\rho_0} g. \quad (2.3b)$$

Here,  $\rho_0$  is a characteristic value of the density of the fluid. Assuming that the base flow is quiescent, we now introduce perturbations (indicated by ') so that  $(u, w) = (u', w')$ ,  $\rho = \bar{\rho}(z) + \rho'$  and  $p = \bar{p}(z) + p'$ . To satisfy the base state, we need a hydrostatic balance given by  $\bar{p}_z = -\bar{\rho}(z)g$ . Equations (2.2) and (2.3) are linearized by assuming that the perturbations are infinitesimal. We use a stream function formulation so that the velocity field satisfies equation (2.1) directly. Therefore,  $u' = -\psi_z$  and  $w' = \psi_x$  where  $\psi$  is the stream function. The linearized equations are as follows:

$$\frac{\partial \rho'}{\partial t} = -w' \frac{d\bar{\rho}}{dz}, \quad (2.4a)$$

$$\frac{\partial u'}{\partial t} = -\frac{1}{\rho_0} \frac{\partial p'}{\partial x} + \nu \nabla^2 u', \quad (2.4b)$$

$$\frac{\partial w'}{\partial t} = -\frac{1}{\rho_0} \frac{\partial p'}{\partial z} + \nu \nabla^2 w' - \frac{\rho'}{\rho_0} g. \quad (2.4c)$$

We now eliminate  $p'$  from equations (2.4b) and (2.4c) to obtain:

$$(\nabla^2 \psi)_t = \nu (\nabla^4 \psi) - \frac{1}{\rho_0} \frac{\partial \rho'}{\partial x} g. \quad (2.5)$$

Finally, eliminating  $\rho'$  from equation (2.4a) and (2.5), we obtain a single equation in terms of the stream function (Sutherland (2010)) as follows:

$$(\nabla^2 \psi)_{tt} + N(z)^2 \psi_{xx} = \nu (\nabla^4 \psi)_t. \quad (2.6)$$

In the above equation,  $N(z)$  is the Brunt-Väisälä frequency (also known as buoyancy

frequency) given by  $N(z) = \sqrt{(-g/\rho_0)d\bar{\rho}/dz}$ . It is the natural frequency of oscillation of fluid parcels that undergo infinitesimal disturbances. In this thesis, a non-uniform stratification is referred to the case when  $N(z)$  is not constant. In other words, a non-uniform stratification is the one wherein  $\bar{\rho}(z)$  varies non-linearly.

### 2.1.1 Dispersion Relation

To obtain insight into the propagation of internal waves, we now consider the inviscid case with a uniform stratification that has a buoyancy frequency  $N_0$ . Equation (2.6) allows plane wave solutions of the form  $\psi = \exp(i(kx + mz - \omega t))$ . Substituting this expression, we obtain the following dispersion relation:

$$\omega^2 = N_0^2 \left( \frac{k^2}{m^2 + k^2} \right) = N_0^2 \sin^2 \theta. \quad (2.7)$$

$\theta$  in the above expression is the angle that the wavenumber vector  $\vec{k} = (k, m)$  makes with the vertical.

An interesting aspect of this dispersion relation is that it does not depend on the magnitude of the wave vector. As a consequence of this, the phase velocity  $\vec{c}_p = (\omega/|\vec{k}|^2)\vec{k}$  and the group velocity  $\vec{c}_g = \nabla_{\vec{k}} \omega$  are perpendicular to each other. Thus, for linear internal waves, energy propagates in a direction that is perpendicular to the phase velocity. Additionally, a given forcing frequency  $\omega$  and buoyancy frequency  $N_0$  fixes the propagation angle irrespective of the magnitude of the wavenumber vector. Propagating internal waves exist only when  $\omega < N_0$ . For  $\omega > N_0$ , the waves are evanescent that do not have any energy flux associated with them.

## 2.2 Problem Formulation

We consider the two-dimensional configuration presented in figure (2-1). The physical domain extends from  $-\infty$  to  $+\infty$  in the  $x$  direction, localized velocity forcing is applied at  $z = 0$ , and internal waves generated by this forcing can propagate downwards freely through  $z = z_1$ . Although the method is applicable to arbitrary stratifications,

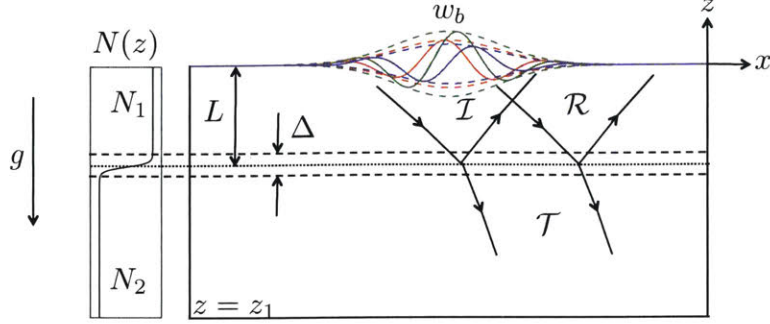


Figure 2-1: Sketch of the physical system. The colored solid lines indicate the vertical velocity forcing function at times  $t_-$  (red),  $t_0$  (green) and  $t_+$  (blue) such that  $t_- < t_0 < t_+$ . The dotted lines indicate the corresponding Gaussian envelopes. Solid lines with arrows define approximate boundaries of the internal wave packets, while the arrows indicate the direction of the group velocity.

to begin we consider a buoyancy frequency profile  $N(z)$  that changes from a value of  $N_1$  to  $N_2$  through a transition layer of thickness  $\Delta$  that lies a distance  $L$  below  $z = 0$ . In this thesis, we will refer to the region above this transition layer as the upper layer and the one below as the lower layer. More specifically, the form of the stratification profile that is considered for our case study in chapter (3) is:

$$N(z) = \left( \frac{N_1 + N_2}{2} \right) + \left( \frac{N_1 - N_2}{2} \right) \tanh \left( \frac{z + L}{\Delta/6} \right). \quad (2.8)$$

The profile given by equation (2.8) is chosen such the buoyancy frequency attains the values  $N_1$  and  $N_2$  at  $z = -L + \Delta/2$  and  $z = -L - \Delta/2$  respectively to within 0.1%. An example profile is indicated in figure (2-1). A similar profile has been used in previous studies (Mathur & Peacock (2009), Ghaemsaidi (2015)) to study the transmission of internal waves through non-uniform stratifications. It has been shown that when the stratification changes are not gradual enough (that is, in this case  $\Delta$  is small enough), internal waves can get reflected and refracted, which is analogous to transmission of light through mediums of different refractive indices. The incident, reflected and transmitted wave packets are indicated in figure (2-1). The problem of interference between the reflected waves and the boundary forcing has been studied by Ghaemsaidi (2015). We thus choose this specific problem to understand the effect

of localization on the interference that has been already studied.

To investigate the effects of spatiotemporal localization, we consider a vertical velocity forcing function given by:

$$w_b(x, t) = \text{Re} \left\{ A \exp(i(k_0 x - \omega_0 t)) \exp\left(\frac{-(x - x_0)^2}{2\sigma_x^2}\right) \exp\left(\frac{-(t - t_0)^2}{2\sigma_t^2}\right) \right\}. \quad (2.9)$$

The function (2.9) can be viewed as a traveling wave of amplitude  $A$  modulated by Gaussian envelopes in both space and time that attain their peak values at  $x = x_0$  and  $t = t_0$ , respectively; the modulation broadens the wavenumber and frequency content of the wave field around  $k_0$  and  $\omega_0$ , depending on the magnitude of the widths of the Gaussian functions given by  $\sigma_t$  and  $\sigma_x$  respectively. This is indicated in figure (2-2). It is to be noted that if the forcing is harmonic (that is,  $\sigma_t, \sigma_x \rightarrow \infty$ ), the Fourier spectra would just be a delta function at  $(k_0, \omega_0)$ . For our studies, since we wish to expand the Fourier spectra, the function given by equation (2.9) is chosen as it allows us an individual control on how wide the spectrum can be in both the spatial and temporal sense. This, however, does not change the dominant wavenumber and frequency hence keeping the phase and group velocity of the resulting internal wave packets the same.

The form of the forcing function at times before, at and after the temporal Gaussian peak is illustrated in figure (2-1). The phase velocity has the magnitude  $\omega_0/k_0$  and is directed to the right. The forcing will thus induce an incident, rightward propagating wave packet ( $\mathcal{I}$ ) with a downward group velocity. This wave packet then experiences reflection ( $\mathcal{R}$ ) and transmission ( $\mathcal{T}$ ) as a result of encountering the transition layer.

As the forcing is provided in the form of the vertical velocity, we take a derivative of equation (2.6) in the  $x$  direction and obtain the following governing equation for the vertical velocity field:

$$(\nabla^2 w)_{tt} + N(z)^2 w_{xx} = \nu (\nabla^4 w)_t. \quad (2.10)$$

Since the domain is infinite in  $x$  and  $t$ , no boundary conditions or initial conditions

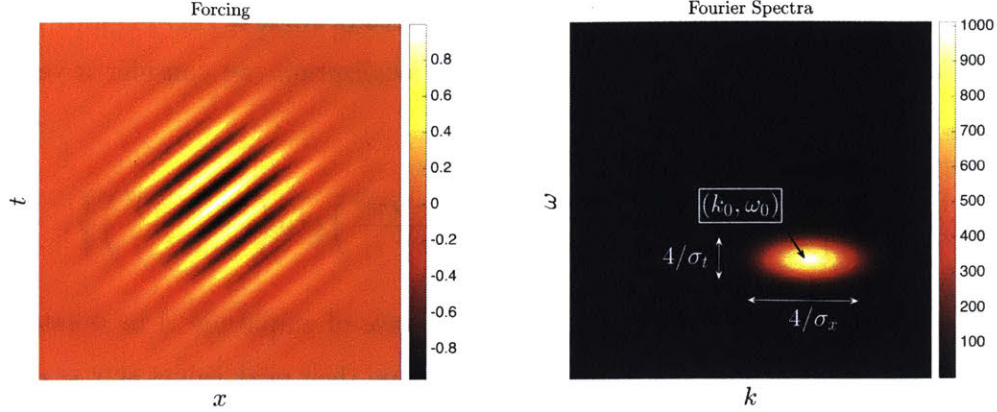


Figure 2-2: An example forcing function and its corresponding Fourier spectra. The left panel indicates the localized nature of the forcing in the spatial dimension  $x$  and the temporal dimension  $t$ . Lines of constant phase have the same slope in the entire domain. The right panel indicates the Fourier spectra of this forcing. It is a Gaussian blob with a peak at  $(k_0, \omega_0)$ . Its widths are inversely proportional to  $\sigma_t$  and  $\sigma_x$ .

are needed along those dimensions. Along  $z$ , the forcing boundary condition needs to be satisfied at  $z = 0$ . At  $z = z_1$ , the bottom of the domain, boundary conditions are implemented in a manner that allows for the internal waves to pass through freely. This is discussed in detail in the next section.

## 2.3 Solution Procedure by Fourier Decomposition

We solve equation (2.10) by performing a Fourier decomposition of the forcing function along  $x$  and  $t$ . This can be done as the forcing function is localized in  $x$  and  $t$  and the domain along both the dimensions is effectively infinite. A general vertical velocity forcing function can be expressed in terms of its Fourier modes as follows:

$$w_b(x, t) = \int_{-\infty}^{+\infty} \int_{-\infty}^{+\infty} \hat{w}_b e^{i(kx - \omega t)} dk d\omega. \quad (2.11)$$

For each Fourier mode  $\hat{w}_b$  of the forcing, we substitute an ansatz  $\hat{w}(z) \exp(i(kx - \omega t))$  for  $w(x, z, t)$  in equation (2.10) to obtain (Ghaemsaidi *et al.*, 2016a):

$$\hat{w}_{zzzz} + \left( \frac{i\omega}{\nu} - 2k^2 \right) \hat{w}_{zz} + k^2 \left( k^2 + \frac{i\omega}{\nu} \left( \frac{N(z)^2}{\omega^2} - 1 \right) \right) \hat{w} = 0. \quad (2.12)$$

This equation gives us the vertical structure of the velocity field for every Fourier mode of the forcing. As noted by Mathur & Peacock (2009), it is not favorable to solve this equation as an initial value problem because it has a pair of rapidly decaying and growing solutions, which can cause numerical instability. It is thus solved as a boundary value problem with two boundary conditions each at  $z = 0$  and  $z = z_1$ . This is done by finding  $m$  such that  $\exp(mz)$  satisfies equation (2.12) in the regions where  $N(z)$  is constant. In the case where a constant stratification is not completely achieved, the application of this method requires the following WKB (Wentzel-Kramers-Brillouin) condition (Cheng (2007)) to be reasonably satisfied at  $z = 0$  and  $z = z_1$ , where the boundary conditions will be applied (Ghaemsaïdi *et al.*, 2016a):

$$|m| \gg \left( \frac{k^2 N N'}{\omega^2} \right)^{1/3}. \quad (2.13)$$

This condition essentially ensures that the vertical wavelength of the internal waves is much smaller than the length-scale of changes in the buoyancy frequency. As a result, the internal waves don't really feel the changes in the background stratification.

In general, there can be four complex roots for  $m$ , the imaginary part of which is the local vertical wavenumber. Only one of these solutions leads to a downward group velocity and a downward weak viscous decay. We choose this root in each layer and express  $\hat{w}(z)$  at the top and bottom as:

$$\hat{w} = \begin{cases} I \exp(m_1 z) + R \exp(-m_1 z) & \text{at } z = 0, \\ T \exp(m_2 z) & \text{at } z = z_1. \end{cases} \quad (2.14)$$

Here,  $I$ ,  $R$  and  $T$  are the amplitudes of the incident, reflected and transmitted waves through the transition layer, respectively, and  $m_1$  and  $m_2$  are the local complex-valued vertical wavenumbers in the  $N_1$  and  $N_2$  layers, respectively. The signs of the terms in the exponential functions are chosen so as to ensure the correct direction of phase

propagation. The following boundary conditions are applied:

$$\widehat{w} = \widehat{w}_b \text{ at } z = 0, \quad (2.15a)$$

$$\widehat{w}_{zz} = m_1^2 \widehat{w} \text{ at } z = 0, \quad (2.15b)$$

$$\widehat{w}_z = m_2 \widehat{w} \text{ at } z = z_1, \quad (2.15c)$$

$$\widehat{w}_{zz} = m_2^2 \widehat{w} \text{ at } z = z_1. \quad (2.15d)$$

The boundary condition given by equation (2.15a) ensures that the vertical velocity at  $z = 0$  is specified by the forcing. Equations (2.15b), (2.15c) and (2.15d) ensure the exponential  $z$  dependence of the excited internal waves that is specified by equation (2.14). If  $z_1 \rightarrow -\infty$ , equation (2.15d) is indeed a redundant condition. However, it closes the system numerically where we have to solve the problem for a finite bottom.

The decomposition given by equation (2.11) is performed discretely using the FFT algorithm. Thereafter, equation (2.12), utilizing the boundary conditions (2.15), is solved numerically using the MATLAB *bvp4c* for the obtained discrete Fourier modes of the forcing. After obtaining the vertical structures  $\widehat{w}(z; \omega, k)$  for every Fourier mode, we transform them back to the space-time domain to obtain the vertical velocity field  $w(x, z, t)$ . The other field variables such as the stream function  $\psi$ , horizontal velocity  $u$  and pressure  $p$  can be found via the linear modal relations:

$$\widehat{\psi}(z) = \frac{\widehat{w}}{ik}, \quad (2.16a)$$

$$\widehat{p}(z) = \frac{\rho_0 \omega \widehat{\psi}_z}{k}, \quad (2.16b)$$

$$\widehat{u}(z) = -\widehat{\psi}_z. \quad (2.16c)$$

Finally, to obtain the field variables we take the inverse Fourier transform of the modal quantities computed for all the discrete forced Fourier modes. The results of using this theoretical solution procedure will be discussed for a test case in chapter 3.

This method of Fourier decomposition works if the excited velocity field is also

localized. That is, its magnitude goes to zero at the end of the simulation time in the entire domain. The Fourier representation in  $x$  and  $t$  implicitly enforces periodic boundary conditions on the velocity field. However, through the bottom boundary condition, we allow for the waves to escape. When the waves are propagating ( $\omega < N_1, N_2$ ), the simulation end time and the domain size in  $x$  need to be chosen such that all of the wave energy escapes through the bottom without reaching the side-ends of the domain. If this is not the case, due to the intrinsic periodic nature of using Fourier modes, there can be spurious waves appearing at the start of the simulation time.

A problem also arises when  $N_2 < \omega < N_1$ . This implies that the waves are propagating in the upper layer but evanescent in the lower layer. We discuss this specific scenario as it is encountered in the lab experiments that are discussed in chapter (4). Because the internal waves cannot propagate through the lower layer, they undergo multiple reflections off the transition layer and the upper boundary. All of the forced input energy then gets focused in the upper layer. There is no mechanism for the energy to escape through the bottom of the domain. The only way by which the wave energy can progressively decrease is through viscous dissipation. Solutions to equation (2.12) ensure that there is viscous decay along the direction of propagation of the internal waves (Ghaemsaidi (2015)). Therefore, the domain size in  $x$  has to be large enough so that the waves decay entirely until they reach the end of the domain. Subsequently, we also conclude that for this particular scenario, the method of Fourier decomposition cannot provide us with an inviscid solution.

## 2.4 Numerical Model

To support our semi-analytic modeling, we use a finite volume numerical model that solves the fully nonlinear Navier-Stokes equations with the Boussinesq approximation (Ueckermann *et al.* (2015)). The Stokes equation is solved by an incremental pressure correction scheme (Ferziger & Peric (2001)) and the advection fluxes are obtained using a TVD (Total Variation Diminishing) scheme.

The internal waves are forced through a partial forcing i.e. only the vertical

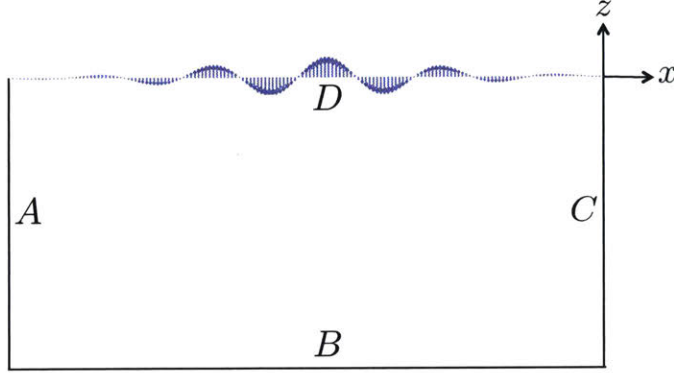


Figure 2-3: The domain used for the nonlinear simulations. No-slip or zero-valued Dirichlet boundary conditions are applied at the boundaries A, B and C. At the top boundary D, the vertical velocity is set to the forcing function as indicated and the horizontal velocity is set to zero. Arrows indicate the forcing velocity vectors.

velocity is forced at the top boundary by setting it to the function given by equation (2.9). Zero-valued Dirichlet boundary conditions are used for other variables at all other boundaries. It has been shown by Mercier *et al.* (2010) that forcing internal waves partially does not introduce any discernible differences in the spectral nature of the velocity fields. The background stratification is introduced as an initial condition in the solver and the time-dependent perturbation density is obtained by subtracting the background density.

A lab-scale simulation was set up to verify our semi-analytic model. The size of the domain was 0.45 m in depth and 2.5 m in span. The number of grid points in  $x$  was 300 and in  $z$  was 100. Adhering to the CFL (Courant-Friedrichs-Lewy) condition, a  $\Delta t$  of  $10^{-3}$  s was chosen. A forcing amplitude of  $10^{-5}$  m/s was used to ensure that the waves are in the linear regime.

# Chapter 3

## Theoretical Results

In this chapter, with the help of a case study, we demonstrate the results of our semi-analytic linear model. In section (3.1), the parameters chosen for this case study are discussed in detail. The resulting velocity field is then compared with the results from the numerical model for validation. A parametric study to explore the effects of spatiotemporal localization is presented in section (3.2). Certain characteristic length scales and time scales that govern the magnitude of the effects of interference are also proposed in this section. We then finally present our conclusions from this analysis in section (3.3).

### 3.1 Validation Case Study

We begin by considering an inviscid system with the stratification parameters  $\Delta/L = 0.5$  and  $N_2/N_1 = 0.6$ , wave field parameters  $\omega_0/N_1 = 0.52$  and  $k_0L = 4.8$ , and localization parameters  $\sigma_t N_1 = 15$  and  $\sigma_x/L = 2$  (here, we use the time scale  $1/N_1$  and length scale  $L$  to non-dimensionalize the localization parameters for convenience only. The correct non-dimensionalization of  $\sigma_x$  and  $\sigma_t$  is discussed in section (3.2)). For these parameters, the spatiotemporal nature of the forcing and vertical velocity field as obtained from the semi-analytic model are presented in figure (3-1). At the time instant shown, the forcing has already occurred and has excited a wave packet  $\mathcal{I}_1$  that has interacted with the transition layer to result in the reflected wave packet  $\mathcal{R}_1$

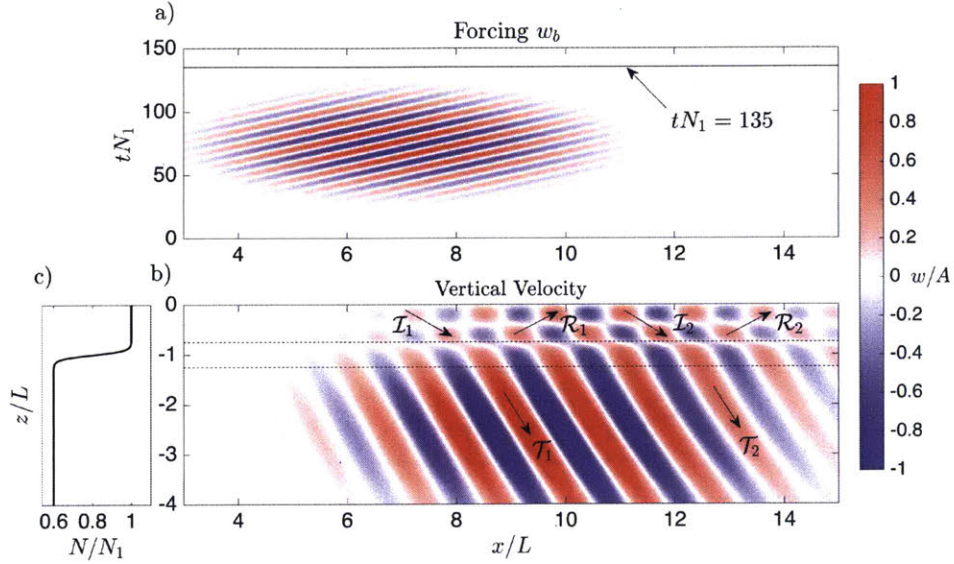


Figure 3-1: Forcing and the excited vertical velocity field for validation case study at  $tN_1 = 135$ . a) Spatiotemporal nature of the velocity forcing at  $z = 0$ , wherein the horizontal line indicates the current time. b) Vertical velocity field in the domain at the current time. The arrows indicate the group velocities of the respective wave packets. c) Stratification or the buoyancy frequency profile. Dotted lines in panel b indicate the transition region of the stratification.

and transmitted wave packet  $\mathcal{T}_1$ . It is clear that the waves in the upper and the lower layer propagate at different angles. In the region of lower buoyancy frequency, the internal waves propagate at a shallower angle. This is consistent with the dispersion relation given by equation (2.7). The wave packet  $\mathcal{R}_1$  then interferes with the forcing at  $z = 0$  and gets reflected back towards to the transition layer as the wave packet  $\mathcal{I}_2$ . This wave packet gets transmitted through the transition layer as  $\mathcal{T}_2$  and reflected as  $\mathcal{R}_2$ . If the forcing was harmonic in time and space, the amplitude of the subsequently resultant incident wave packets (represented by  $\mathcal{I}$ ) would be non-negligible for an infinite number of such reflections. However, due to the spatiotemporal localization, we observe that the amplitude has greatly decreased even for the second reflected wave packet  $\mathcal{R}_2$ .

We now define the transmission parameter for this system to be  $\tau_w = \{\max|w|/A \text{ at } z/L = -1 - 0.5\Delta/L\}$ , that is the ratio of the maximum excited vertical velocity just below the transition region and the forced vertical velocity amplitude  $A$ .

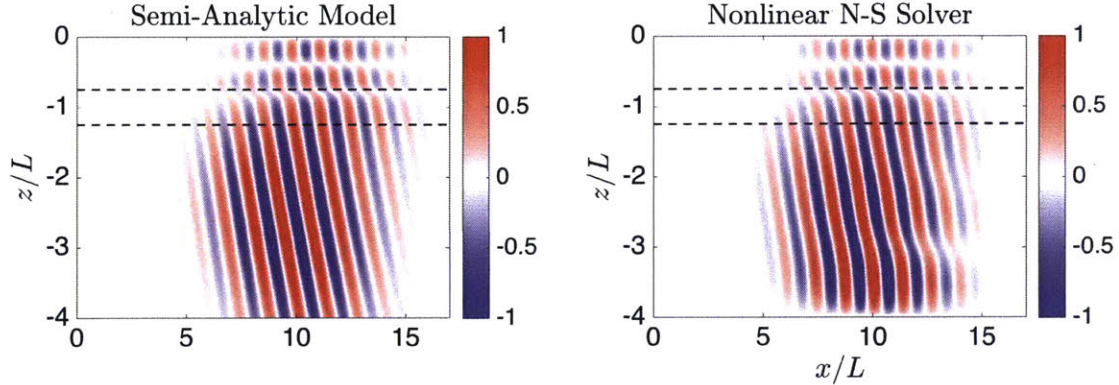


Figure 3-2: Comparison of the semi-analytic and numerical vertical velocity field normalized by the forcing amplitude ( $w/A$ ) at  $tN_1 = 135$ . The dotted lines in both the panels indicate the transition region of the background stratification

For this example,  $\tau_w$  is determined to be 1.56; for comparison, for a harmonic forcing (that is,  $\sigma_t, \sigma_x \rightarrow \infty$ ) with the same forcing parameters the transmission parameter is  $\tau_w = 2.53$  ( $\approx 62\%$  larger), indicating a higher degree of constructive interference. This can be corroborated by identifying that at the time the bulk of the reflected wave packet  $\mathcal{R}_1$  reaches  $z = 0$ , the forcing has a diminished amplitude both due to the spatial and temporal localization. This reduces the amount of interference that can happen between the reflected wave packet and the forcing itself in the upper layer. One can also think of it from the frequency and wavenumber domain. Due to the localization, we introduce a band of wavenumbers and frequencies which have their own coefficients of transmission for this system. The total coefficient of transmission is the weighted sum of these transmission coefficients where the weights are the relative Fourier amplitudes. If the dominant wavenumber and frequency lie on a harmonic transmission peak, the transmission for a localized forcing is expected to be lower due to the contribution of wavenumbers and frequencies around that do not lie on the harmonic transmission peak.

### 3.1.1 Comparison with Numerical Model Results

As a validation for the semi-analytic model, we now compare the velocity field obtained with the results from the numerical model discussed in chapter (2). Figure

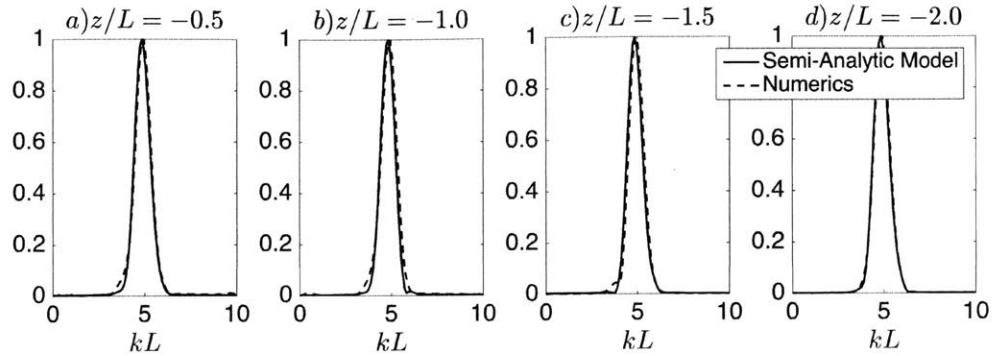


Figure 3-3: Comparison of the normalized Fourier spectra of the vertical velocity obtained from the semi-analytic model and numerics (for the same parameters as in figure (3-1) with  $tN_1 = 135$ ). Panel (a): above the transition layer, panel (b): inside the transition layer and panels (c, d): below the transition layer.

(3-2) shows that the vertical velocity field obtained for the parameters discussed earlier from the linear semi-analytic model and the numerical model agree well with each other. Above the transition region, the wave field is a result of multiple incident and reflected waves as indicated in figure (3-1). This effect is captured well by both the models. Near the bottom of the domain, there are some deviations in the numerical wave field as compared to the semi-analytic model. These deviations can be attributed to the no-slip boundary conditions implemented on all the boundaries which leads to wave reflections. The boundary conditions in the semi-analytic model, however, allow for the waves to freely escape through the bottom of the domain.

For a more quantitative validation, we compare the normalized Fourier spectra of the vertical velocity field at different depths as obtained from the semi-analytic model and numerical simulations for this case study. This comparison is presented in figure (3-3). There are very small differences in the spectra at depths above, inside and slightly below the transition region. This does not affect the Fourier spectrum of the waves transmitted well below the transition layer, however, for which there is very good agreement between both the models.

With this validation in hand, we are free to use the semi-analytic model to perform parametric studies to investigate how the forcing parameters affect the transmission of the system. Intuitively, we expect that as the size of the forcing gets larger both

spatially and temporally, effects of interference will be enhanced as more number of reflections can now interfere with the forcing (figure (3-1)). This would also depend on the dominant frequency and wavenumber, however, as the propagation angle and the group velocity of the waves depends on these factors. Using the linear semi-analytic model, we investigate this dependency in the next section.

## 3.2 Effects of Spatiotemporal Localization

Using a ray approach for a discontinuous stratification profile, it has been shown by Ghaemsaïdi (2015) that as the number of interactions between the reflected waves and the boundary forcing increases, the effect of either constructive or destructive interference becomes more profound. In the case of a spatially localized forcing, only a finite number of reflections actually interact with the forcing and, similarly, if the forcing is temporally localized the time for which the forcing exists only permits a limited number of reflections to interfere. Adopting this perspective, we will define a characteristic length scale  $L^*$  and a time scale  $t^*$ , with a view to developing a practical criteria for when interference effects will be evident.

### 3.2.1 Criteria for Possible Interference Effects

Consider figure (3-4), which shows a ray path of internal waves that have the dominant wavenumber and frequency  $(k_0, \omega_0)$  of the forcing. These waves propagate as a group along a direction that makes an angle  $\theta_0$  with the horizontal.  $\theta_0$  is given by  $\theta_0 = \sin^{-1}(\omega_0/N_1)$  according to equation (2.7). Further utilizing equation (2.7), the group speed along this direction is given by:

$$c_g = |\nabla_{\vec{k}}\omega| = (N_1 \sin \theta_0 \cos \theta_0)/k_0. \quad (3.1)$$

As indicated in figure (3-4), the ray path that originates at the  $z = 0$  level traverses a distance  $L_0$  before reaching the center of the transition layer. By geometry,  $L_0 = L/\sin \theta_0$ . After getting reflected from the transition layer, it traverses a distance of

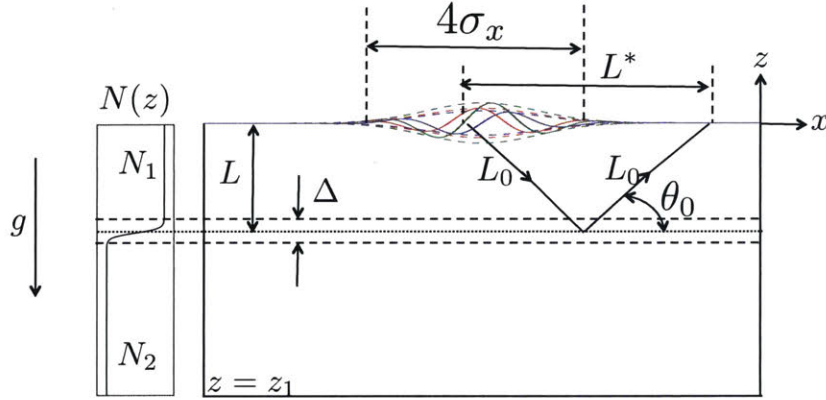


Figure 3-4: Sketch of the physical system overlaid with the length scale  $L^*$  and the distance  $L_0$ . Arrows associated with the waves indicate the direction of the group velocity.

$L_0$  until it reaches the  $z = 0$  level again. At this stage, the reflected waves can again interfere with the forcing. We now define  $L^*$  as the horizontal distance between the point at which a wave packet leaves the  $z = 0$  level and the point at which it comes back after getting reflected from the transition region. Furthermore,  $t^*$  is defined as the time it takes for the wave packet to traverse the path length  $2L_0$ . Therefore, these scales are given by the following expressions:

$$L^* = 2L \cot \theta_0, \quad (3.2a)$$

$$t^* = (2L_0)/c_g = (2k_0L)/(N_1 \sin^2 \theta_0 \cos \theta_0). \quad (3.2b)$$

Equation (3.2a) is obtained using geometry and equation (3.2b) is obtained by utilizing the fact that the interval waves move through a distance  $2L_0$  at their group speed  $c_g$  given by equation (3.1).

The length scale  $L^*$  indicates the horizontal distance away from the point of origin of the waves where the first interference can potentially take place with the forcing. Similarly,  $t^*$  indicates the time after the waves originate at which the first interference might occur. The effect of the interference thus depends on the magnitude of the forcing itself at distance  $L^*$  and a time  $t^*$  away. To quantify this, we define the

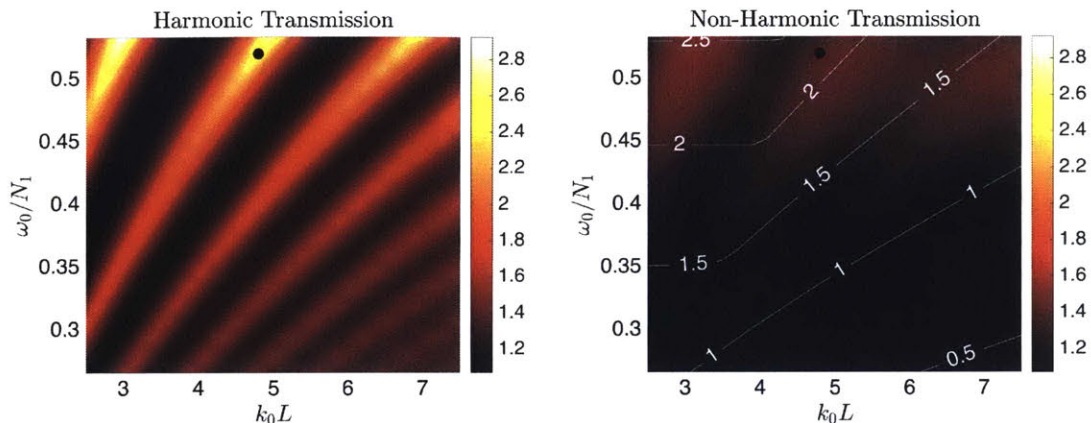


Figure 3-5: Comparison of the transmission parameter (for  $\Delta/L = 0.5$ ,  $N_2/N_1 = 0.6$ ) in the harmonic and non-harmonic case. The left panel shows the transmission parameter for harmonic forcing. The black circles in both the panels indicate the forcing parameters considered for the motivating example. The right panel shows the transmission parameter for a localized forcing with  $\sigma_t N_1 = 22.5$ ,  $\sigma_x/L = 2$ .

following dimensionless parameters:

$$n_x = 4\sigma_x/L^*, \quad (3.3a)$$

$$n_t = 4\sigma_t/t^*, \quad (3.3b)$$

where  $n_x$  and  $n_t$  reasonably quantify the number of reflections the spatiotemporal extent of the forcing supports for interference; the factor of 4 ensures that 95% of the forcing amplitude is considered. It is to be expected that interference effects present in the case of harmonic forcing will be evident only when both  $n_x$  and  $n_t$  are above a certain threshold. For interference to take place between the reflected waves and the forcing at least once, we expect  $n_x, n_t > 1$  for any transmission peaks or troughs to be evident.

### 3.2.2 Comparison of Harmonic and Non-Harmonic Transmission

We consider the results for the transmission parameter  $\tau_w$  for the harmonic and non-harmonic forcing, presented in figure (3-5). For a harmonic forcing, the transmission

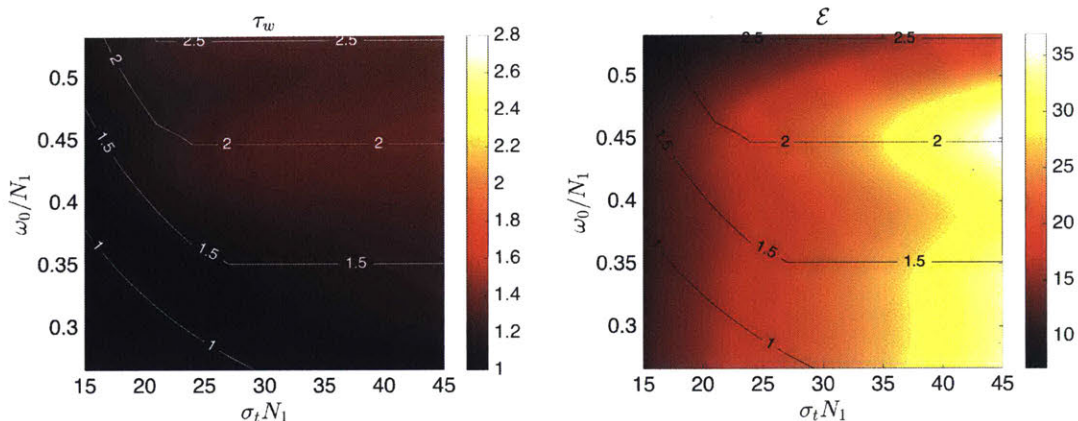


Figure 3-6: Effect of temporal delocalization on the transmission parameter and the total energy transferred (for  $\Delta/L = 0.5$ ,  $N_2/N_1 = 0.6$ ,  $\sigma_x/L = 2$ ,  $k_0L = 4$ ). The color bar in the left panel is set to be the same as in figure (3-5). The contours in both the panels correspond to the function  $\min\{n_x, n_t\}$ .

peaks and troughs can be clearly seen, achieving maximum values of  $\tau_w \sim 3$ . In contrast, the transmission plot for the localized forcing, which is overlaid by contours of the function  $\min\{n_x, n_t\}$ , displays identifiable peaks only when  $n_x, n_t > 1$ ; below this threshold, the transmission peaks disappear (i.e. there needs to be enough spatiotemporal extent for at least one reflected wave packet to interfere with the forcing). Furthermore, the maximum value of the transmission parameter is notably reduced to  $\tau_w \sim 1.5$ . Parameters for the case study discussed earlier are indicated by black circles in figure (3-5). It is clear that if the forcing were harmonic, the frequency and wavenumber pair lies on a transmission peak. In the case of a non-harmonic forcing, the localization reduces the effect of either constructive or destructive interference. Thus, if the harmonic system undergoes destructive interference, the transmission parameter for the non-harmonic forcing would be expected to increase and vice versa. The case study under consideration has a frequency and wavenumber that exhibits constructive interference in the harmonic forcing case. Therefore, expectedly, the transmission parameter reduces in the non-harmonic case.

The non-harmonic transmission plot in figure (3-5) has been plotted for fixed spatial and temporal size of the forcing viz.  $\sigma_x$  and  $\sigma_t$ . We now look at the scenario where the spatial nature of the forcing is fixed and only the temporal part (i.e. the

parameters  $\omega_0$  and  $\sigma_t$ ) is changed. Figure (3-6) presents results for the vertical velocity transmission parameter,  $\tau_w$ , and the energy input to the system,  $\mathcal{E}$ , for a disturbance of spatial nature ( $k_0L = 4, \sigma_x/L = 2$ ) and varying temporal extent ( $15 < \sigma_t N_1 < 45$ ). The total energy input (per unit distance in the  $y$  direction) is calculated as  $\mathcal{E} = \int \int (pw) dx dt$  and has been non-dimensionalized by the characteristic value  $\rho_0 A^2 L^2$ . As the forcing is specified in terms of the vertical velocity, the energy input to the system is expected to vary with the forcing parameters. For  $\sigma_t N_1 \approx 15$ , there is a trivial change in the transmission parameter and the energy input as a function of  $\omega_0/N_1$ , but as  $\sigma_t N_1$  exceeds 25, constructive peaks and destructive troughs due to interference emerge. Contours of the function  $\min\{n_x, n_t\}$  are overlaid on both plots and again it is evident that peaks and troughs in both the transmission parameter and the energy input appear only above  $n_x, n_t > 1$ .

### 3.3 Conclusions

In this chapter, we have validated our semi-analytic linear model by comparing the results with a nonlinear numerical model. This has allowed us to use the numerically cheap linear model to perform parametric studies in order to investigate the effects of spatiotemporal localization on the transmission of internal waves. It has been shown that such a localization does have an impact on the degree of either constructive or destructive interference that takes place in the system. This is directly reflected by a decrease or increase in the transmission parameter respectively. We have also proposed relevant length and time scales that govern whether or not interference effects will be evident. A practical criteria based on these scalings has been shown to meaningfully identify whether interference effects are evident. It is to be noted that the proposed criteria does not in itself indicate whether there is interference in a given physical system. The criteria gives us information on whether these effects due to interference would be evident if they are present in the case of a harmonic forcing.



# Chapter 4

## Experiments

In this chapter, we describe the laboratory experiments that were performed to test the theoretical predictions discussed in chapter 3. We begin by describing the experimental apparatus in section (4.1). Given a stratification, there are essentially four parameters that affect the transmission parameter. These are: two spatial parameters (dominant wavenumber and spatial size of the forcing) and two temporal parameters (dominant frequency and temporal size of the forcing). As is described in section (4.2), internal waves were forced using a wave generator that is made of discrete plates moving up and down. In this section, experimental limitations that allowed us the flexibility to change only the temporal parameters are further discussed. The results we obtained from our experiments are discussed in section (4.3), wherein the method used to calculate the experimental transmission parameter is discussed in section (4.3.1). We compare the experimental and theoretical transmission parameter and present a discussion on the experimental velocity fields in section (4.3.2).

### 4.1 Apparatus

For the experimental studies, we used a glass wave tank that is 5.5 m long, 0.55 m wide and 0.55 m high. The schematic of front view of the setup is shown in figure (4-1). A photograph of the actual experimental setup is shown in figure (4-2). The tank was separated by a partition that ran along its length creating a working section

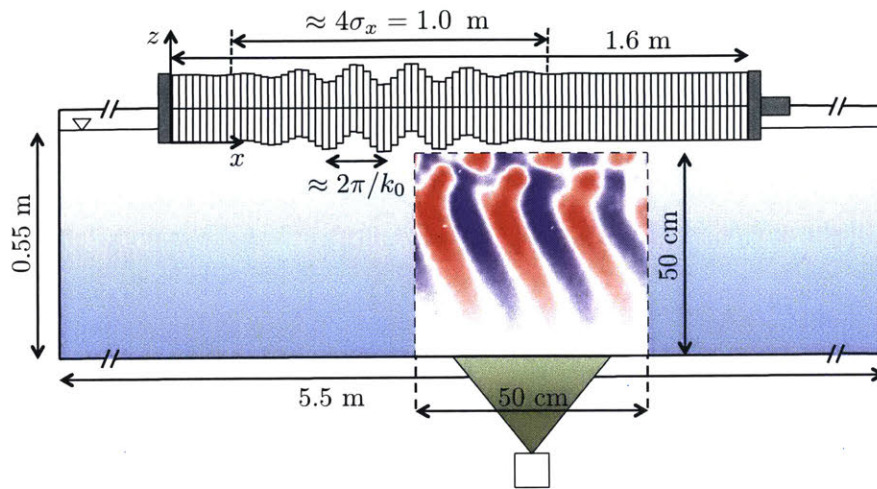


Figure 4-1: Schematic of the front view of the experimental setup. The observation region is indicated by dotted lines and it is illuminated from underneath the tank by the LASER sheet (depicted in green).

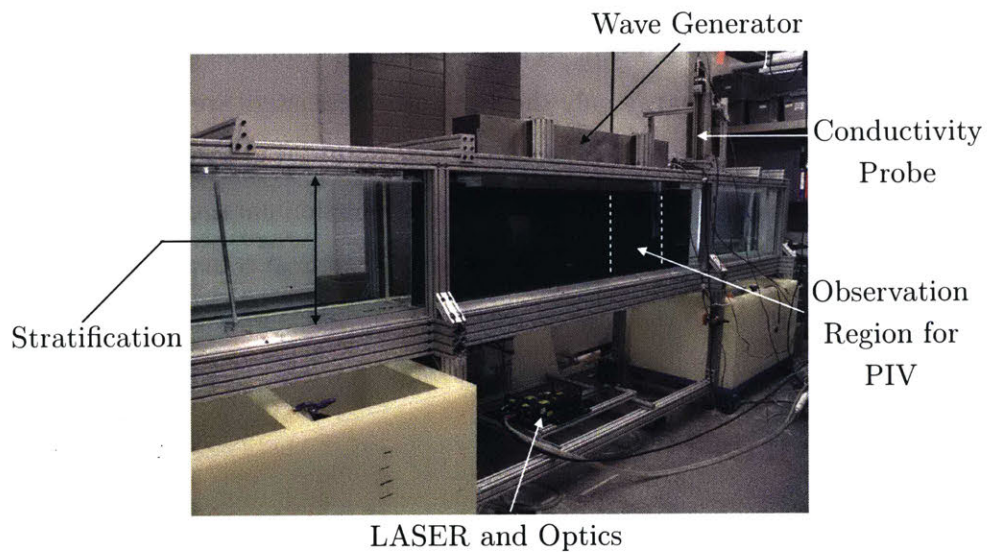


Figure 4-2: Actual experimental setup indicating all the important components

which was 0.2 m wide. There were parabolic reflectors at the ends of the tank that reflected any waves that were generated in the working section of the tank so that they were dissipated behind the partition (Echeverri, 2009).

Salt-densified water was used to set up the density stratification using the double-bucket method, for which the flow rates out of the two buckets were controlled using two peristaltic pumps. The flow rate from the dense water bucket to the freshwater bucket and that from the freshwater bucket to the experimental tank were maintained at 3 lpm and 6 lpm (where lpm stands for liters per minute). As a result of the stratification, density in the tank varied between 1000 kg/m<sup>3</sup> and 1040 kg/m<sup>3</sup>. A Precision Measurements Engineering conductivity probe was calibrated and used to measure the density profile. The calculated buoyancy frequency from the raw density profile is plotted in figure (4-3). This profile differs a little from the profile given by equation (2.8). The small bump in the buoyancy frequency just above the transition region occurred due to experimental limitations of changing the volumes of water in the buckets in the double-bucket method. Nevertheless, we account for this difference by fitting a function of the following form:

$$N(z) = \left( \frac{N_1 + N_2}{2} \right) + \left( \frac{N_1 - N_2}{2} \right) \tanh \left( \frac{z + L}{\Delta/6} \right) + (N_3 - N_1) \exp \left( -\frac{1}{2} \left[ \frac{z + L}{\Delta/6} \right]^2 \right). \quad (4.1)$$

This function is essentially the one defined by equation (2.8) superimposed with a Gaussian function in the transition region. The parameters:  $N_1$ ,  $N_2$ ,  $N_3$ ,  $\Delta$  and  $L$  are obtained by performing a least squares fit to the experimental data. As is shown in figure (4-3), this function approximates the experimental buoyancy frequency profile very well and is thus used for predictions from the semi-analytic model.

The velocity field of the generated internal waves was measured using PIV in a 50 cm × 50 cm observation region as indicated in figure (4-1). Hollow glass spheres with a diameter of 8 – 10 μm were used to seed the flow. As indicated in figure (4-1) and (4-2), a light sheet was created from underneath the tank using a pulsed Nd:YAG laser. Images of the seeding particles were recorded using an Imager Pro X 4M LaVision CCD camera at a resolution of 2042 × 2042 and at a rate of 32

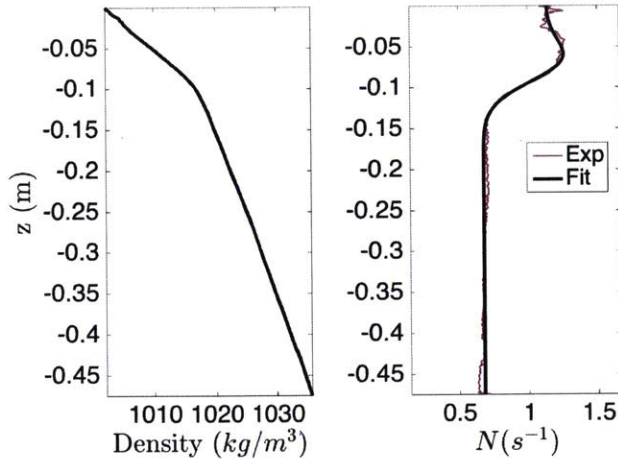


Figure 4-3: Experimental stratification profile. The left panel indicates the density variation that is measured using the conductivity probe. The right panel shows the buoyancy frequency profile obtained by numerical differentiation of the raw density profile. The fitted analytic function to this profile is also indicated.

images per forcing period. Since the flow velocities are of the order of a few mm/s, a single laser head was pulsed and cross-correlation was performed between consecutive particle images. The post-processing and calibration of the cameras was done using the DaVis PIV software developed by LaVision. An example experimental vertical velocity field overlaid on the experimental schematic is indicated in figure (4-1).

## 4.2 Wave Generator Configuration

In order to force the internal waves, we used a wave generator that has been built based on the design by Gostiaux *et al.* (2007) and later analyzed by Mercier *et al.* (2010). The wave generator was set up on top of the tank as shown in figures (4-1) and (4-2). It consisted of 84 individual plates whose vertical position is controlled by individual circular cams whose centers can be offset from the spindle center. The eccentricity ( $e_j$ ) and phase ( $\phi_j$ ) of the cams were adjusted individually, where  $j$  indicates the serial number of the plates. The eccentricities  $e_j$  were set to a maximum value of  $e = 5$  mm. The cams are attached to a spindle that was rotated by a motor at variable speed (angular position of the spindle is given by  $\gamma(t)$ ). The time dependent vertical velocity

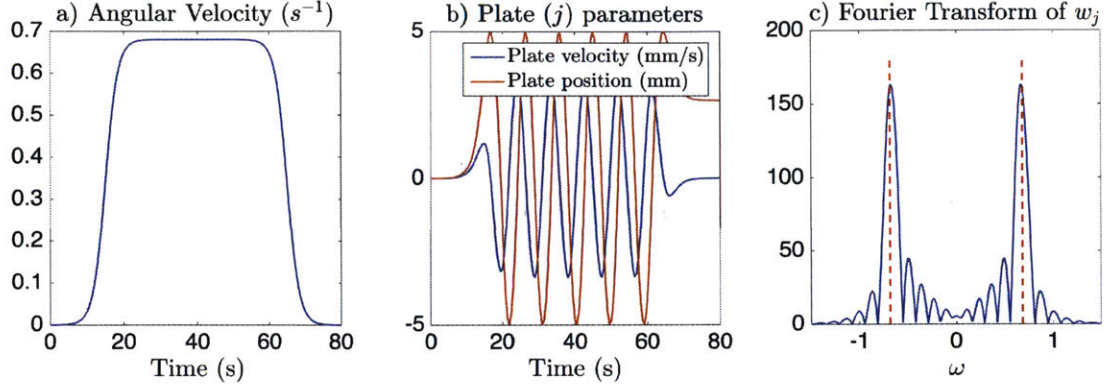


Figure 4-4: An example of the temporal part of the wave generator forcing given by equation (4.3). Panel a shows the angular velocity ( $d\gamma/dt$ ) of the motor for the following set of experimental parameters:  $\omega_0 = 0.68 \text{ s}^{-1}$ ,  $\sigma_t = 50 \text{ s}$ ,  $t_0 = 40 \text{ s}$ ,  $\delta = 20 \text{ s}$ ,  $e = 5 \text{ mm}$ . Panel b indicates the vertical position and velocity of a single generator plate. Panel c shows the amplitude of the Fourier Transform of the plate vertical velocity  $w_j$ , wherein the dotted red lines indicate  $\pm\omega_0$ .

of each plate can be expressed as:

$$w_j(t) = e_j \cos(\phi_j + \gamma(t)) d\gamma/dt. \quad (4.2)$$

The wave generator provided two degrees of freedom in the horizontal spatial direction (eccentricity and phase) but only one in time ( $\gamma(t)$ ). Hence, getting a temporally localized velocity profile that is smooth was non-trivial. Also, to set the wave generator to realize a specific spatial profile, all of the plates and cams need to be removed and configured individually. This limited our ability to vary the spatial parameters of the forcing through an experiment. Therefore, we chose to fix the spatial profile and vary the temporal parameters alone viz. frequency and time window of the forcing. The spatial Gaussian envelope of the idealized forcing function given by equation (2.9) was physically realized by setting  $e_j = e \exp(-(x_j - x_0)^2/2\sigma_x^2)$  and  $\phi_j = k_0 x_j$ . Since the rotation of all the cams is given by a single function  $\gamma(t)$ , however, it was not possible to exactly reproduce the temporal part of the function in equation (2.9). We thus utilized the following function for  $\gamma(t)$ , such that  $d\gamma/dt$

forms a localized temporal envelope:

$$\gamma(t) = \frac{\omega_0}{2} \int_0^t \left[ \tanh\left(\frac{\bar{t} - (t_0 - \sigma_t/2)}{\delta/6}\right) - \tanh\left(\frac{\bar{t} - (t_0 + \sigma_t/2)}{\delta/6}\right) \right] d\bar{t}. \quad (4.3)$$

Such a definition ensured that  $\gamma(t)$  changes monotonically and hence the phase speed was always directed in the same direction. The phase speed of the forcing did not remain constant, however, but increased to a maximum value of  $(\omega_0/k_0)$  in a time  $\delta$ . It stayed at the maximum value for a time of about  $\sigma_t$  and reduced back to zero in  $\delta$ . Nevertheless, such a  $\gamma(t)$  profile gave us a temporally localized forcing with a broad frequency spectrum close to but not exactly  $\omega_0$ . The forcing is also symmetric about the time  $t_0$  which we will refer to as the mean time of the forcing. An example angular velocity ( $d\gamma/dt$ ) profile is shown in figure (4-4). The Fourier Transform of the plate velocity indicates that it has a peak at  $\pm\omega_0$  and is fairly symmetric about the peak. The function given by equation (4.3) thus served as an adequate function for verifying our theoretical predictions.

The stepper motor on the wave generator was controlled using a LabView program and an NI (National Instruments) motion controller to attain the intricate  $\gamma(t)$  profile. For the experimental runs, the wave generator was configured such that  $k_0 = 40.69 \text{ m}^{-1}$  and  $\sigma_x = 0.25 \text{ m}$  and  $\omega_0$  and  $\sigma_t$  were varied. The choice of  $k_0$  was made so as to ensure that the Reynolds number associated with the excited waves is not too small that viscous effects are highly dominant. A large value of  $k_0$  would result in a larger viscous dissipation as the viscous decay rate is proportional to  $k_0^3$  (Ghaemsaidi (2015)). For the chosen value of the wavenumber, the Reynolds number,  $Re = A\omega_0/\nu k_0$  was of the order of (10 – 100).

### 4.3 Results

For the stratification that was set up, we performed a total of 43 experimental runs where only the temporal part of the forcing that is given by  $\gamma(t)$  in equation (4.3) was varied. The value of  $\delta$  was arbitrarily set to 20s by ensuring that this value

| $\sigma_t$ (s) | $\delta$ (s) | $t_0 = 5 + (\sigma_t + \delta)/2$ (s) |
|----------------|--------------|---------------------------------------|
| 20             | 20           | 25                                    |
| 50             | 20           | 40                                    |
| 200            | 20           | 115                                   |

Table 4.1: Values chosen for temporal forcing parameters:  $\sigma_t$ ,  $\delta$  and  $t_0$  for the experiments.

was larger than the typical buoyancy period in all the experiments. The dominant frequency  $\omega_0$  was varied from  $0.68\text{s}^{-1}$  to  $1.28\text{s}^{-1}$  for three different values of  $\sigma_t$  viz. 20, 50 and 200 s. This range of frequencies was especially chosen so that the internal waves in the bottom layer are evanescent. Such a scenario ensures that all of the forced energy is concentrated in the upper layer, thus leading to resonant peaks of transmission (Ghaemsaidi (2015)). The value of the mean time  $t_0$  was chosen on the basis of  $\sigma_t$  (detailed values are show in table (4.1)). To better resolve the expected peaks in the transmission parameter for  $\sigma_t = 200$  s, we performed experiments for 21 different values of  $\omega_0$  that were equally spaced in the specified range. For  $\sigma_t = 20$  s and 50 s, 11 values of  $\omega_0$  were used each.

### 4.3.1 Transmission Studies

In order to calculate the transmission parameter from the experimental data, the vertical velocity field at a depth just below the transition region (that is, at  $z = -L + \Delta/2$ ) was analyzed. The top 0.01% data values over all times and horizontal distances at this depth were found and divided by the forcing amplitude  $A\omega_0$ . The transmission parameter was defined as the mean of these values and the standard deviation provided a rough error estimate for the experimentally measured transmission. This method ensured that the measured transmission was not based on a single data value. The choice of using the top 0.01% was arbitrary and made so as to ensure that sufficient number of data values were actually considered for this calculation without substantially lowering the transmission value due to averaging.

Figure (4-5) shows the experimentally obtained transmission for the experiments we performed for 43 different sets of  $\omega_0$  and  $\sigma_t$ . Additionally, the theoretical

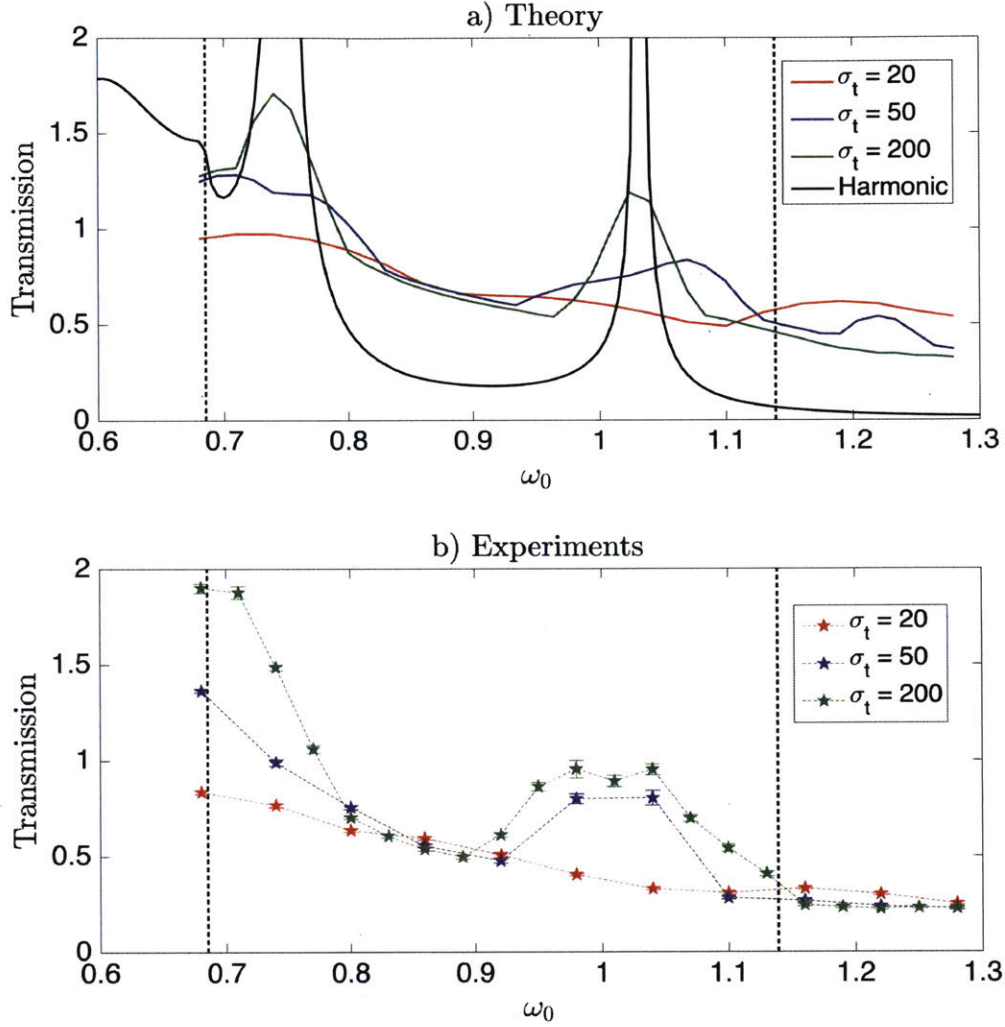


Figure 4-5: Theoretical and experimental transmission for different values of the temporal parameters  $\sigma_t$  and  $\omega_0$ . In panel a, the red, blue and green solid lines indicate the transmission computed by using the semi-analytic model for a spatiotemporally localized forcing. The solid black line indicates the transmission for a harmonic forcing ( $\sigma_x, \sigma_t \rightarrow \infty$ ). In panel b, the star markers are the experimental transmission values with the colors corresponding to the respective  $\sigma_t$  values. The vertical dotted lines in both the panels indicate the buoyancy frequencies in the lower and upper layer ( $N_2$  and  $N_1$ ).

transmission curves for spatiotemporally localized forcings and a harmonic forcing ( $\sigma_t, \sigma_x \rightarrow \infty$ ) are plotted. These were obtained from the semi-analytic model discussed in chapter 2.

### 4.3.2 Discussion

For the theoretical curves in figure (4-5), the transmission peaks are taller and the troughs are deeper for higher values of  $\sigma_t$ . This is consistent with the results discussed in chapter 3. The peaks and troughs are, however, not as strong as the ones for a harmonic forcing. For the lowest time window for  $\sigma_t = 20$  s, no evidence of either constructive or destructive interference is seen as the transmission varies monotonically with  $\omega_0$ .

The experimental transmission values follow a similar trend as the theoretical curves. In regions of constructive interference, the transmission value for experiments with higher  $\sigma_t$  that is, a larger forcing time window, is higher. These transmission peaks are observed around  $\omega_0 \approx 0.7 \text{ s}^{-1}$  and  $\omega_0 \approx 1.0 \text{ s}^{-1}$ .

Figure (4-6) shows the vertical velocity fields for  $\omega_0 = 0.68 \text{ s}^{-1}$  when the transmission of internal waves is amplified due to constructive interference between the reflected waves and the forcing. It is evident from the magnitude of the vertical velocity that for  $\sigma_t = 200$  s, internal waves undergo maximum amplification at the mean time  $t_0$  of the forcing. This is a direct result of multiple interactions between the reflected waves and the forcing that a larger forcing time window allows. For lower values of  $\sigma_t$ , the maximum amplitude of the vertical velocity is reduced. For later times, instabilities are seen to arise in the case of  $\sigma_t = 200$  s which lead to a reduction in the vertical length scale of the excited velocity field. This can be attributed to the development of Parametric Subharmonic Instability (PSI) due to wave-wave interactions. PSI effectively transfers energy from longer to shorter length scales. This has been earlier reported in similar physical systems by Ghaemsaïdi *et al.* (2016*b*). This might be a reason behind the enhanced transmission at frequencies close to  $\omega_0 \approx 0.7 \text{ s}^{-1}$ . Occurrence of PSI allows for the leakage of energy to the bottom layer as the daughter waves have a frequency that is lower than the parent frequency. We

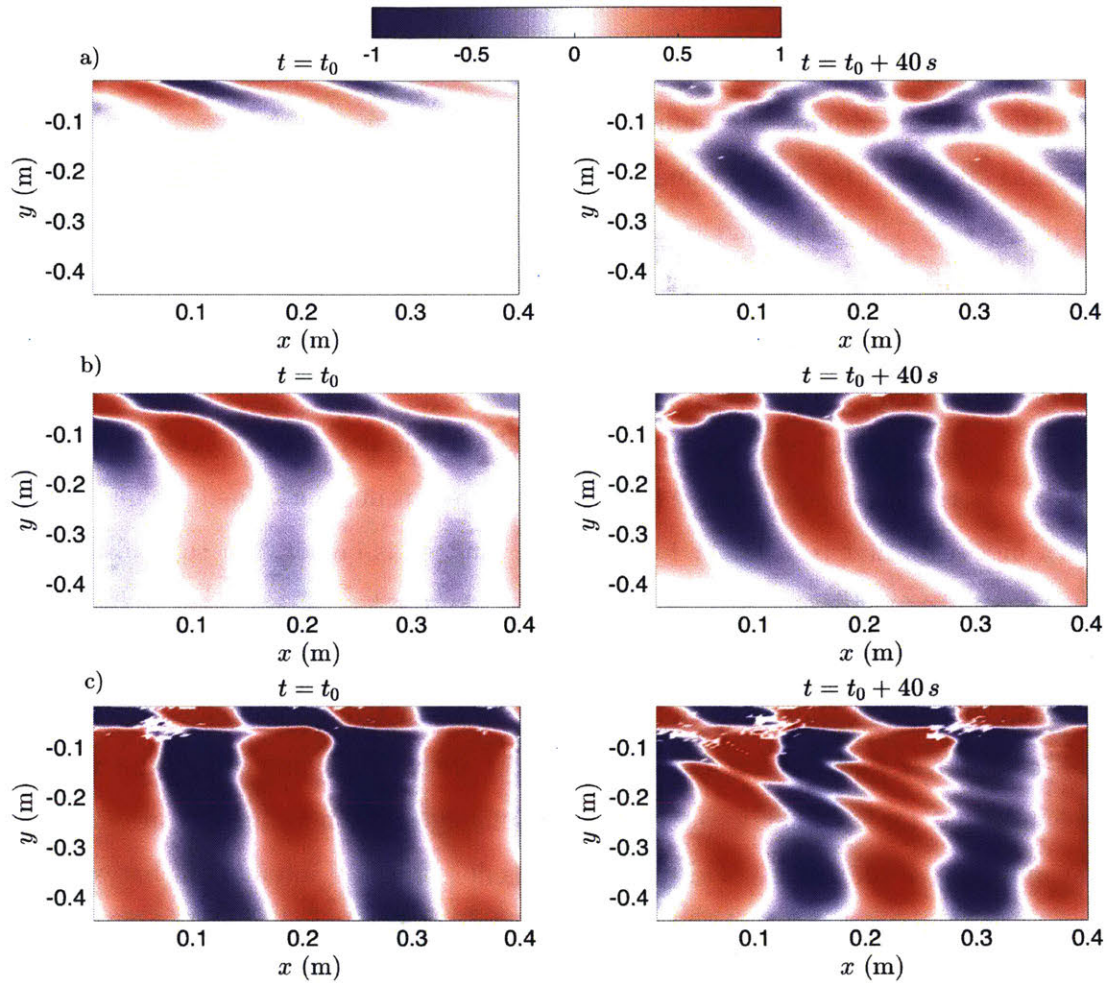


Figure 4-6: Plots of the experimental vertical velocity field normalized by the forcing amplitude ( $w/(A\omega_0)$ ). All the panels indicate velocity fields forced at  $\omega_0 = 0.68 \text{ s}^{-1}$ , a frequency at which resonance occurs. Rows a, b and c indicate velocity fields for  $\sigma_t = 20, 50$  and  $200$  s respectively. The left and right panels of each row correspond to the velocity field at the time  $t_0$  (about which the angular velocity is symmetric) and at  $40$  s after  $t_0$ .

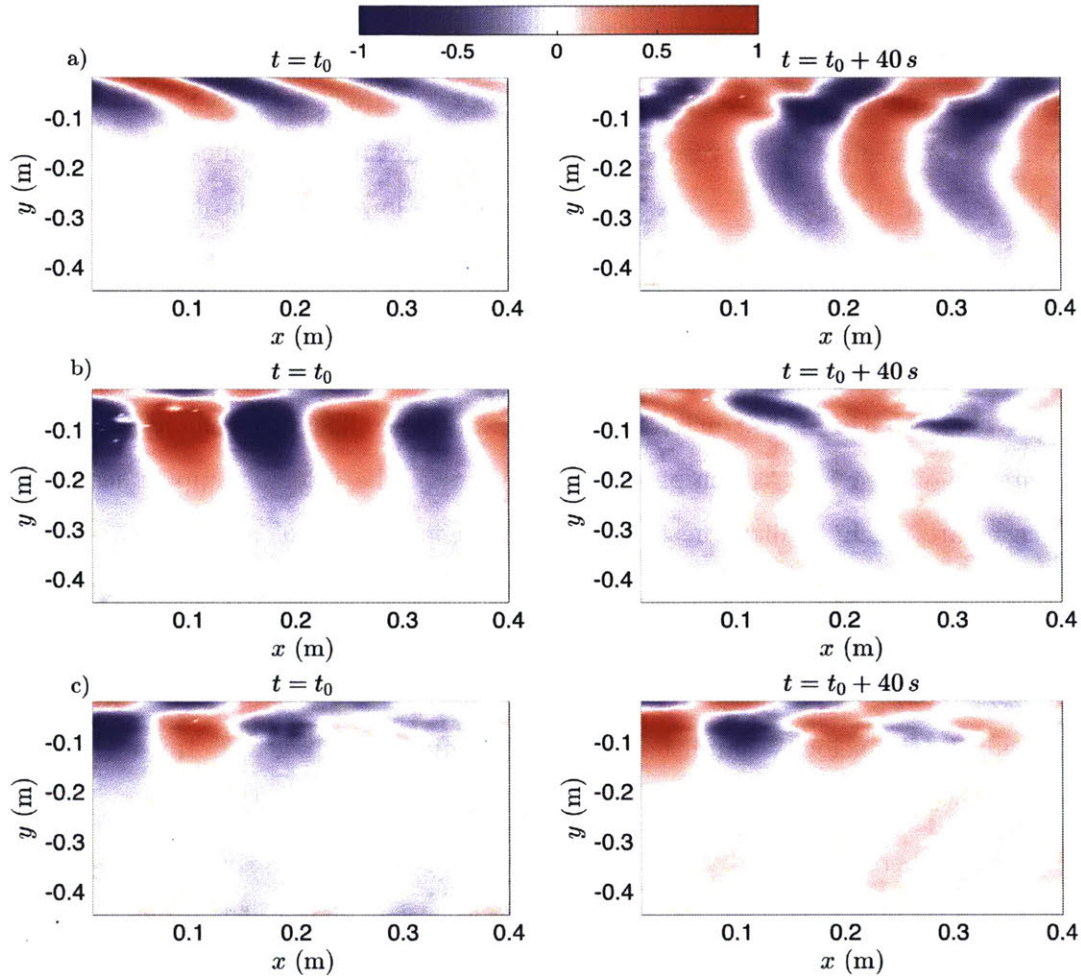


Figure 4-7: Plots of the experimental vertical velocity field normalized by the forcing amplitude ( $w/(A\omega_0)$ ). All the panels indicate velocity fields forced at  $\omega_0 = 0.86 \text{ s}^{-1}$ , a frequency at which diminution occurs. Rows a, b and c indicate velocity fields for  $\sigma_t = 20, 50$  and  $200 \text{ s}$  respectively. The left and right panels of each row correspond to the velocity field at the time  $t_0$  (about which the angular velocity is symmetric) and at  $40 \text{ s}$  after  $t_0$ . The color scale is the same as in figure (4-6).

also note that since we are considering time-localized forcings, the internal wave field contains a band of frequencies that can potentially lead to wave-wave interactions. However, when the forcing is highly localized, despite the frequency band being large, there is not enough time for the instabilities to grow. This is why PSI does not occur when  $\sigma_t = 20$  s.

In the diminution regions around  $\omega_0 \approx 0.85 \text{ s}^{-1}$  and  $\omega_0 \approx 1.2 \text{ s}^{-1}$  that are evident through the transmission curves in figure (4-5), the transmission values for  $\sigma_t = 200$  s are lower than those for  $\sigma_t = 50$  s, which are in turn lower than those for  $\sigma_t = 20$  s. This provides evidence of larger destructive interference for a larger temporal size of the forcing. The amplification and diminution values are, however, far off from the predictions for a harmonic forcing due to the spatiotemporal localization.

For the scenario of destructive interference at  $\omega_0 = 0.86 \text{ s}^{-1}$ , velocity fields are shown in figure (4-7). As compared to figure (4-6), the velocity amplitudes in all the cases are much smaller due to diminution. For the case of  $\sigma_t = 200$  s, internal waves undergo larger diminution as can be seen by the reduced velocity amplitude as compared to smaller values of  $\sigma_t$ . Contrary to the constructive interference case, instabilities are not developed even at longer time scales. This is due to a significant reduction in the velocity amplitudes thus preventing the growth of any wave-wave interactions.

Overall, there is a good qualitative agreement between the theoretical and experimental results. We now revisit the criteria we had developed in chapter 3 to determine whether the effect of interference is evident. This criteria is based on the dimensionless parameters  $n_x$  and  $n_t$  defined in equation (3.3).  $n_x$  and  $n_t$  quantitatively represent the number of reflections the forcing supports for interference in a spatial and temporal sense. In defining these parameters for the experimental scenario, the spatial size of the forcing is taken to be  $4\sigma_x$  as the factor of 4 ensures that we include 95% of the forcing amplitude in the Gaussian envelope. The temporal part of the forcing, however, does not have a Gaussian envelope but is represented by equation (4.3) where  $\sigma_t$  (without any additional factors) represents the time window for which the forcing is active. Since only the temporal parameters are varied,  $n_x$  re-

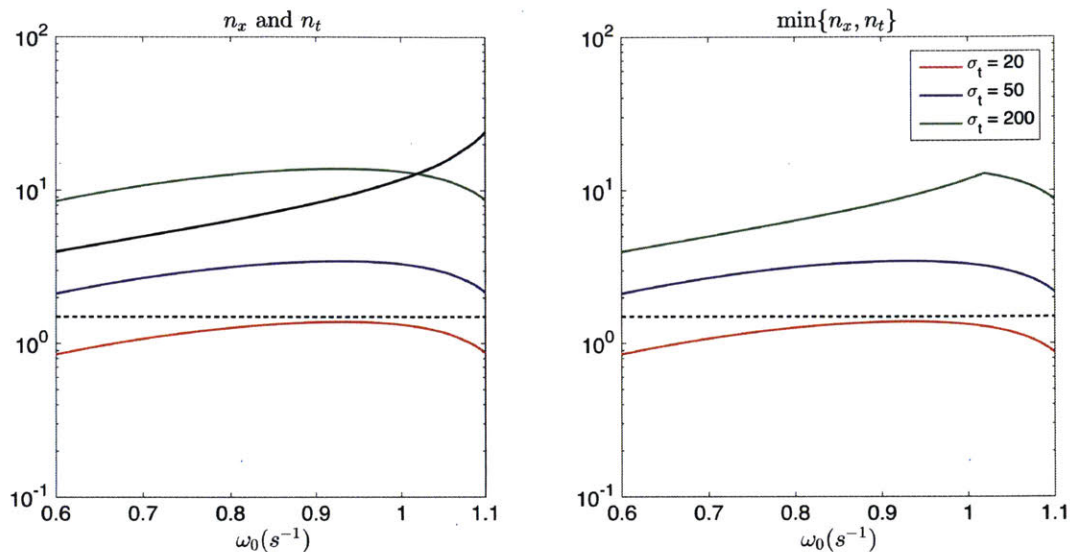


Figure 4-8: Plots of the critical ratios  $n_x$  and  $n_t$ . The left panel presents the plots of  $n_x$  (solid black line) and  $n_t$  (solid colored lines).  $n_t$  is plotted for different values of  $\sigma_t$ . The right panel indicates the minimum of  $n_x$  and  $n_t$ . A log scale is used for the y-axis. In both the panels, the black dotted line indicates the value of 1.5 for reference.

mains the same for different values  $\sigma_t$  but  $n_t$  scales accordingly. These dimensionless parameters are plotted in figure (4-8). It is clear that as the forcing gets de-localized,  $n_t$  increases. For the chosen spatial extent of the forcing,  $n_x$  is well above 1 for all frequencies. The value of  $n_t$ , however, is lower than or close to 1 for  $\sigma_t = 20$  s. According to the results in chapter 3, for any effects of interference to be evident, the minimum of  $n_x$  and  $n_t$  must be reasonably larger than 1. This explains why we do not observe any transmission peaks or troughs for  $\sigma_t = 20$  s. It is to be noted that for the forcing parameters chosen, even if the spatial extent allows for multiple reflections to interfere, the temporal localization becomes the limiting factor for the case of smallest  $\sigma_t$ . For  $\sigma_t = 200$  s, there is a cross-over of the  $n_x$  and  $n_t$  curves. This does not lower the effect of interference as both  $n_x$  and  $n_t$  are well above 1 and thus support either constructive or destructive interference.



# Chapter 5

## Conclusions

In this thesis, we have performed a study of the effect of spatiotemporal localization on the transmission and interference of internal waves in non-uniform stratifications. Motivated by previous studies, we have considered the specific problem of boundary-forced internal waves in non-uniform stratifications. In chapter 1, it was argued that all of the previous studies related to internal wave interference have considered temporally harmonic internal waves. We made the case that since the transmission of internal waves in non-uniform stratifications strongly depends on interference between incident and reflected waves, spatial as well as temporal localization must have a non-negligible impact on the transmission.

To explore the above idea further, we presented an idealized physical problem in chapter 2. We considered a two-layer stratification system with a finite transition layer where the buoyancy frequency changes continuously. This stratified fluid system was forced by a spatiotemporally localized forcing in the vertical velocity at the top boundary. In order to obtain internal wave field solutions for this problem, the semi-analytic model earlier developed by Ghaemsaïdi *et al.* (2016a) was further extended to consider such localized forcings. In this chapter, we also discussed a numerical model for solving the fully nonlinear Navier-Stokes equations that was used for validation purposes.

In chapter 3, we made use of a motivating example to demonstrate how spatiotemporal localization of the boundary forcing causes a significant change in the trans-

mission. This example was also used to compare the internal wave fields obtained from the semi-analytic and the numerical model. Having validated the semi-analytic model, we utilized it to perform parametric studies and analyze the effects of localization on internal wave interference. In this regard, a practical criteria to determine whether the effects of interference would be evident was developed. This criteria is dependent on several parameters such as the temporal and spatial size of the forcing, the depth and buoyancy frequency of the upper layer, and the dominant frequency and wavenumber of the forcing. It essentially quantifies the number of interactions between the reflected waves and the forcing that the spatiotemporal size of the forcing can support. We have developed this criteria with a view of determining how closely the effects of interference for a non-harmonic forcing resemble with those for a harmonic forcing. For the motivating example, it was shown that this criteria meaningfully determines the parametric regimes where transmission peaks or troughs due to constructive or destructive interference are expected. It was also found that there are significant differences in the amount of energy required to force the system with a non-harmonic forcing as opposed to a harmonic one.

In order to demonstrate our theoretical predictions, we performed a set of laboratory experiments that were presented in chapter 4. For a given stratification and a fixed spatial nature of the forcing, we performed experiments for three different values of the temporal size of the forcing over a range of forced frequencies. These experiments were in very good qualitative agreement with the theoretical predictions for transmission. As expected, on temporal de-localization of the forcing, transmission peaks and troughs were seen to get stronger, thus indicating higher degree of constructive or destructive interference. For the experimental parameters, we revisited our criteria from chapter 3 and showed that it correctly explains the experimental results as well.

Overall, this thesis demonstrates that transmission results for internal waves undergoing interferences in non-uniform stratifications can be highly dependent on how spatiotemporally localized they are. For example, a direct implication of our study is that the amount of energy a storm can transfer to the deep ocean through excitation

of internal waves greatly depends on its spatial extent and the amount of time it lasts for. In such cases, performing a harmonic analysis by considering the dominant frequency of the storm can lead to incorrect results. The practical criteria we have developed can be potentially applied to such geophysical scenarios because of the existence of a well-defined pycnocline in the upper ocean in most cases. This provides an estimate for the length scale of the upper layer that plays a crucial role in applying the criteria.

## 5.1 Future Work

The semi-analytic model we have developed for localized forcings could be applied to stratification profiles from the real ocean. In a typical ocean stratification, the depth of the pycnocline below the mixed layer can be taken as a length scale for the criteria we have developed. The criteria can then be utilized to determine whether the effects of interference would be evident. Such an analysis can thus identify the correct length and time scales for an ocean storm to excite internal waves that undergo any interference in the upper ocean.

Extension of this study to more complicated stratifications is another avenue of future research. As discussed in chapter 1, an example of a complex stratification profile is the double-diffusive staircase structure that is prevalent in the Arctic ocean. In such a case, it is unclear what the relevant length scale must be so that the criteria that we have developed could be directly applied. The model we have developed can, however, be applied to such stratification profiles to perform a study to identify the relevant length scale.



# Bibliography

- ALFORD, MATTHEW H, MACKINNON, JENNIFER A, SIMMONS, HARPER L & NASH, JONATHAN D 2016 Near-Inertial Internal Gravity Waves in the Ocean. *Annual review of marine science* **8**, 95–123.
- BAINES, PETER G. & HOINKA, KLAUS P. 1985 Stratified flow over two-dimensional topography in fluid of infinite depth: A laboratory simulation. *Journal of the Atmospheric Sciences* **42** (15), 1614–1630.
- BELL, T H 1975 Lee Waves in Stratified Flows with Simple Harmonic Time-Dependence. *Journal of Fluid Mechanics* **67**, 705–722.
- CHENG, H. 2007 *Advanced Analytic Methods in Applied Mathematics, Science, and Engineering*. LuBan Press.
- CUSHMAN-ROISIN, B. & BECKERS, J.M. 2011 *Introduction to Geophysical Fluid Dynamics: Physical and Numerical Aspects*. Academic Press.
- ECHEVERRI, PAULA & PEACOCK, THOMAS 2010 Internal tide generation by arbitrary two-dimensional topography. *Journal of Fluid Mechanics* **659**, 247–266.
- ECHEVERRI, PAULA M. 2009 Internal tide generation by tall ocean ridges. PhD thesis, Massachusetts Institute of Technology.
- FERZIGER, J.H. & PERIC, M. 2001 *Computational Methods for Fluid Dynamics*. Springer Berlin Heidelberg.
- GHAEMSAIDI, SASAN J. 2015 Interference and resonance of internal gravity waves. PhD thesis, Massachusetts Institute of Technology.
- GHAEMSAIDI, S J, DOSSER, H V, RAINVILLE, L & PEACOCK, T 2016a The impact of multiple layering on internal wave transmission. *Journal of Fluid Mechanics* **789**, 617–629.
- GHAEMSAIDI, S. J., JOUBAUD, S., DAUXOIS, T., ODIER, P. & PEACOCK, T. 2016b Nonlinear internal wave penetration via parametric subharmonic instability. *Physics of Fluids* **28** (1), 011703.
- GILL, A.E. 1982 *Atmosphere-Ocean Dynamics*. Elsevier Science.

- GILL, A E 1984 On the Behavior of Internal Waves in the Wakes of Storms. *Journal of Physical Oceanography* **14** (7), 1129–1151.
- GOSTIAUX, L., DIDELLE, H., MERCIER, S. & DAUXOIS, T. 2007 A novel internal waves generator. *Experiments in Fluids* **42** (1), 123–130.
- KUNDU, PIJUSH K, COHEN, IRA M & DOWLING, DAVID R 2012 *Fluid mechanics*, 5th edn. Waltham, MA Academic Press.
- MATHUR, MANIKANDAN & PEACOCK, THOMAS 2009 Internal wave beam propagation in non-uniform stratifications. *Journal of Fluid Mechanics* **639**, 133–152.
- MATHUR, MANIKANDAN & PEACOCK, THOMAS 2010 Internal wave interferometry. *Physical Review Letters* **104**, 118501.
- MCDUGALL, T.J. & BARKER, P.M. 2011 *Getting started with TEOS-10 and the Gibbs Seawater (GSW) Oceanographic Toolbox*.
- MERCIER, MATTHIEU J, MARTINAND, DENIS, MATHUR, MANIKANDAN, GOSTIAUX, LOUIS, PEACOCK, THOMAS & DAUXOIS, THIERRY 2010 New wave generation. *Journal of Fluid Mechanics* **657**, 308–334.
- NAULT, J. T. & SUTHERLAND, B. R. 2007 Internal wave transmission in nonuniform flows. *Physics of Fluids* **19** (1), 016601.
- ROEMMICH, DEAN & GILSON, JOHN 2009 The 2004-2008 mean and annual cycle of temperature, salinity, and steric height in the global ocean from the argo program. *Progress in Oceanography* **82** (2), 81 – 100.
- SUTHERLAND, BRUCE R. 2010 *Internal Gravity Waves*. Cambridge University Press.
- SUTHERLAND, BRUCE R. & YEWCHUK, KERIANNE 2004 Internal wave tunnelling. *Journal of Fluid Mechanics* **511**, 125–134.
- TIMMERMANS, M.-L., TOOLE, J., KRISHFIELD, R. & WINSOR, P. 2008 Ice-Tethered Profiler observations of the double-diffusive staircase in the Canada Basin thermocline. *Journal of Geophysical Research* **113**.
- TOFFOLI, A., MCCONOCHIE, J., GHANTOUS, M., LOFFREDO, L. & BABANIN, A. V. 2012 The effect of wave-induced turbulence on the ocean mixed layer during tropical cyclones: Field observations on the australian north-west shelf. *Journal of Geophysical Research: Oceans* **117**.
- UECKERMANN, M.P., LIN, JING, SROKA, SYDNEY & LERMUSIAUX, P.F.J. 2015 2.29 Finite Volume MATLAB Framework Documentation. Mseas report. Department of Mechanical Engineering, Massachusetts Institute of Technology, (<http://mseas.mit.edu/?cat=5>).
- WUNSCH, CARL 1975 Internal tides in the ocean. *Reviews of Geophysics* **13** (1), 167–182.

WUNSCH, C & FERRARI, R 2004 Vertical Mixing, Energy and the General Circulation of the Oceans. *Annual Reviews of Fluid Mechanics* **36** (1), 281–314.